

# Micromechanics based fatigue life prediction of a polycrystalline metal applying crystal plasticity

Ke-Shi Zhang<sup>a,\*</sup>, J. Woody Ju<sup>a,b</sup>, Zhenhuan Li<sup>c</sup>, Yi-Long Bai<sup>d</sup>, Wolfgang Brocks<sup>e</sup>

<sup>a</sup> Key Laboratory of Disaster Prevention and Structural Safety, College of Civil and Architectural Engineering, Guangxi University, Nanning 530004, China

<sup>b</sup> Department of Civil and Environmental Engineering, University of California, Los Angeles, CA 90095-1593, USA

<sup>c</sup> Department of Mechanics, Huazhong University of Science and Technology, Wuhan 430074, China

<sup>d</sup> State Key Laboratory of Nonlinear Mechanics (LNM), Institute of Mechanics, Chinese Academy of Sciences, Beijing 100080, China

<sup>e</sup> Institute for Materials Science, Christian Albrecht University, Kiel, Germany

## ARTICLE INFO

### Article history:

Received 26 May 2014

Received in revised form 6 January 2015

Available online 21 February 2015

### Keywords:

Crystal slipping

Cyclic plasticity

Statistical RVE model

Inhomogeneous strain

Symmetrical strain cycle

Low-cycle fatigue life

## ABSTRACT

The fatigue-life of a polycrystalline superalloy under symmetrical cyclic strain controlled loading at a temperature of 650 °C is investigated by numerical simulations on the micro-level, focusing on the inhomogeneous evolution of plastic deformation in a polycrystalline aggregate. A methodology (Zhang et al., 2011, 2013) to predict the low-cycle fatigue life by micro-level simulations along with statistical analysis is applied following the steps: (1) A statistically representative volume element (RVE) consisting of a number of crystal grains is constructed by Voronoi tessellation. Stresses and plastic strains are calculated by a crystal plasticity model including nonlinear kinematic hardening. (2) The RVE is subjected to repeated symmetric tensile-compressive loading. (3) The inhomogeneous stress and strain fields are statistically analyzed during the load cycles. (4) Failure by LCF is strain controlled and occurs if either of the quantities, standard deviation of longitudinal strain in tensile direction, maximum or statistical average of first principal strains in the RVE at the tension peak of cyclic loading reaches a respective critical value. (5) Using the present methodology, a family of failure curves for fatigue lives under different strain amplitudes can be predicted by varying the critical values. Finally, appropriate critical values can be identified by a respective cyclic experiment with only one strain amplitude.

© 2015 Elsevier Ltd. All rights reserved.

## 1. Introduction

The investigations on metal low-cycle fatigue are usually related to metallurgical and mechanical aspects. Namely, the investigations often involve the micro-structure of the metal and its evolution, the response of stress and strain to different loading and the number of load cycles required to cause failure. Therefore, for low-cycle fatigue analysis, the descriptions on the mechanical

behavior related to the microstructure of a metallic material under repeated loading are very important.

The metal fatigue mechanisms and mechanical behavior can be described at different scales and from different viewpoints, depending on which processes at which structural levels researchers choose to focus upon (cf. Manson, 1953; Coffin, 1954; Chaboche, 2008; Shenoy et al., 2008; McDowell and Dunne, 2010; Sangid et al., 2011; Zhang et al., 2013; Keshavarz and Ghosh, 2013; Huang et al., 2014; Sweeney et al., 2013; Sweeney et al., 2014a). Since the processes of fatigue failure in materials usually occur in a very small volume, a microstructural analysis is essential for experimental and computational investigations.

\* Corresponding author.

E-mail addresses: [kszhang2002@hotmail.com](mailto:kszhang2002@hotmail.com), [zhangks@gxu.edu.cn](mailto:zhangks@gxu.edu.cn) (K.-S. Zhang).

Modern technological advances have made this possible, so that we can extend fatigue studies to very small scales or cross scale in order to clarify the role of material microstructure.

Polycrystalline metallic materials consist of a large number of crystal grains. At the grain level, its mechanical behavior is very inhomogeneous, since the grains are randomly orientated and the material properties of an individual grain are anisotropic with respect to elastic and plastic deformations due to its crystal lattice-array. To investigate the evolution of inhomogeneous deformation fields in a metallic material during low cycle fatigue, it is necessary to explore the micro-level plastic deformation and its accumulation, and the law of fatigue life with respect to the cyclic loading conditions. To achieve this objective, it is essential to select a reasonable scale for the analysis, a suitable constitutive model to reflect the cyclic plastic deformation mechanism at a relevant size level, and the corresponding fatigue model for service life analysis.

If the analysis is carried out at scales from  $10^{-3}$  to mm by using a material representative volume element, representing the sizes from a crystal grain to a material test specimen, the results can be verified both qualitatively and quantitatively by using the conventional fatigue test machine and observation instrument (Zhang et al., 2013). For a polycrystalline metal, an appropriate representative element model should be able to describe the material's mechanical behavior at both the macroscale and the microscale. Such a material element contains a considerable number of grains, so that it can statistically reflect the typical material microstructural characteristics and the mechanical responses under realistic experimental conditions. On the other hand, it is adequately small to still represent a “material point” at the macroscale. This representative volume element (RVE) can be constructed by using a Voronoi polyhedron aggregation (Barbe et al., 2001; Kanit et al., 2003; Zhang et al., 2005). It should be emphasized that, different from classical RVE studies, the present RVE is used not only to reflect the homogenized properties but also to study the evolution of the inhomogeneous local deformation of a heterogeneous material (Ju and Chen, 1994; Ju and Tseng, 1996; Ju and Sun, 2001; Sun et al., 2003a,b; Zhang, 2004; Shenoy et al., 2008; Zhang et al., 2013).

The deformation of a crystalline grain in polycrystalline material can be split into the anisotropic elastic lattice distortion and the anisotropic crystal plastic slip caused by a large number of local stress-driven dislocations moving along the close-packed plane of atoms. These deformation mechanisms involving lattice distortion and crystal slip were discussed and investigated through establishing a crystal slip theory by Hill and Rice (1972), and Asaro and Rice (1977). Later, different algorithms under various configurations at finite deformations were suggested (cf. Peirce et al., 1983; Needleman et al., 1985; Kalidindi et al., 1992; Maniatty et al., 1992; Sarma and Zacharia, 1999), mainly to apply the crystal plasticity theory to numerical analysis of texture-forming. Further, improvements in computational schemes were made, in which the Cauchy stress was chosen as a basic variable and a

mixed implicit and explicit algorithm matched to a user material subroutine of ABAQUS was established (Zhang, 2004; Zhang et al., 2005). In recent years, a Voronoi polyhedron aggregation has increasingly been employed for the analysis of three-dimensional microscopic inhomogeneous stress and strain fields of polycrystalline materials. The activation and development of different slip systems of each grain in the RVE, driven by the local stress, can be computed by taking account of the random grain orientations.

In order to understand the deformation evolution process in a heterogeneous metal at the micro-level under the low-cycle fatigue loading, suitable computations need to be performed to describe the material microstructural features, the microscale deformation mechanism and the variance of strains and stresses in a metal during the low-cycle loading process. To take into account the Bauschinger effect in a single crystal, which is important for fatigue analysis due to cyclic loading condition, Cailletaud (1992) introduced the back-stress and nonlinear kinematic hardening into the slip description at the level of each slip system. Subsequently, Hutchinson's power law (Hutchinson, 1976) was generalized by introducing the back stress into a crystal plasticity model (Feng et al., 2004), in which the Armstrong–Frederick type kinematic hardening rule (Armstrong and Frederick, 1966) was invoked to capture the Bauschinger effect. Moreover, for the purpose of accommodating the cyclic hardening feature of the slipping system, a modified evolution law for the back-stress with respect to the resolved shear stress on slip system was proposed by Zhang et al. (2011), by which the inhomogeneous deformation of a copper under cyclic loading and the subsequent yield of an aluminum after cyclic loading are studied by Zhang et al. (2013) and Hu et al. (2015), respectively.

The strains and stresses in a metallic material at the microscale are usually inhomogeneous due to the heterogeneity of the material's microstructure. At the micro-level, the inhomogeneity and heterogeneity for the microstructure and the deformation distribution will evolve with the loading cycles. As a result, a material changes gradually due to the evolution of residual deformations and stresses and the orientations and shapes of the grains. In order to characterize the evolution of material structure and behavior at various micro-scales, many investigations have been engaged (Abdeljaoued et al., 2009; Dunne et al., 2007; Guilhem et al., 2010; Taheri et al., 2011; Przybyla and McDowell, 2010; Dingreville et al., 2010; Sweeney et al., 2013; Sweeney et al., 2014b; Zhang et al., 2011). In the process of a material deformation under cyclic loading, the evolutions of the material inhomogeneity may continue until the fatigue failure occurs, which can be described by statistical distribution with two characteristic parameters; i.e., the mean value and standard deviation (Zhang et al., 2013).

A primary objective to investigate fatigue is to establish a rational methodology for fatigue life prediction. Here, the fatigue life means the cycle number to failure of a material specimen under cyclic loading with a macro uniform deformation. The Manson–Coffin equation (Manson, 1953; Coffin, 1954) or its modification was widely used

by some researchers to predict fatigue life of materials (Ni and Mahadevan, 2004; Buciumeanu et al., 2011; Roy et al., 2012; Wu et al., 2014; Ince and Glinka, 2014). But the premise for using this equation is that a series of fatigue experiments of the material needs to be carried out to obtain the respective fitting parameters in the equation. In order to seek for more rational damage models, different fatigue indicator parameters (FIPs) were suggested to assess fatigue failure (Ye and Wang, 2001; Jiang et al., 2009; Chaboche et al., 2012; Naderi et al., 2013). The investigations by Manonukul and Dunne (2004), Sweeney et al. (2013) and Guerchais et al. (2014) were conducted by analyzing crystal plasticity at the grain level considering the accumulation of plastic slip. In some investigations the length-scale effect and cross scale analysis for fatigue were taken into account (Sweeney et al., 2013; Sweeney et al., 2014a; Dunne, 2014). Furthermore, a multi-scale energy based criterion was proposed, by which the energy for persistent slip band (PSB) was estimated at both continuum and atomistic scales (Sangid et al., 2011).

Similar to the Manson–Coffin equation, these models need a series of fatigue experiments to optimally fit the corresponding parameters prior to its application. Zhang et al. (2013) suggested a methodology focusing on the evolution of deformation inhomogeneity of a metal at the grain level, in which the micro strain fluctuation of a material characterized by using the statistical standard deviation is employed to assess the material fatigue law. The key advantage is that the methodology has only one parameter to be determined for fatigue crack initiation by which the fatigue law can be characterized. In the present paper, this method will be verified through the analysis of fatigue life of a superalloy and further investigated with respect to the determination of a fatigue indicator parameter.

## 2. Objective and Methodology

The present paper aims at verifying and improving the methodology proposed by Zhang et al. (2013). The fatigue life of a nickel-based superalloy, GH4169, under strain-controlled cyclic loading with varying amplitudes will be analyzed. The inhomogeneous evolution of plastic deformations in a polycrystalline aggregate is calculated by a crystal plasticity model including nonlinear kinematic hardening and analyzed. The polycrystalline aggregate is constructed by Voronoi tessellation and supposed to be statistically representative for the microstructure of the material.

### 2.1. Modeling the material as statistically representative volume element

The investigated material GH4169 is a precipitation-strengthened nickel-based superalloy with a grain size of about 10–30  $\mu\text{m}$ , and its precipitation-strengthening phase particles are much smaller than the grain. Similar to other superalloys, it contains the phases  $\gamma$ ,  $\gamma'$ ,  $\gamma''$  and MC carbides. Its matrix phase is face-centered cubic (fcc) (Li et al., 2013). Its plastic deformation on the micro-scale

can be described by slipping along the respective slip-systems of the lattice of individual grains.

From the macroscopic viewpoint, a material point or element is regarded as a small continuum particle with uniform mechanical properties. Any real material exhibits a heterogeneous microstructure, however, causing non-uniform local stress and strain fields. Therefore, stress and strain distributions are inhomogeneous at the microscale even if the material is strained under uniform loading at the macroscale. Variations in stress and strain occur not only in various grains but also within the same grain due to intergranular constraint. During cyclic fatigue loading these effects will accumulate and the stretch and shear deformations in a local region may reach a much higher value than the externally applied strain amplitude. The fatigue failure of the material depends on the strain and stress variances at the grain level.

Fig. 1 shows a schematic of a small cube taken from a macroscopic specimen, which is regarded as a representative volume element (RVE) consisting of a number of grains. For simplification, it is assumed that the mechanical properties are the same for all grains and that no cracks or voids are present in the polycrystal. Due to their much smaller size, the precipitation-strengthening particles are ignored. Using this RVE, the inhomogeneous deformation process in a metallic material under external cyclic loading can be analyzed. The true grain structure of GH4169 is exhibited by a SEM image in Fig. 2 (Li et al., 2013), and the histogram of the grain area ratio within the material is shown in Fig. 3, in which the area ratio of grain area and the area average,  $a/a_{\text{average}}$ , is taken from the SEM image.

As displayed in Fig. 4, the present RVE consists of  $30 \times 30 \times 30 = 27,000$  eight-node hexahedral elements and 29,791 nodes. The surfaces are planes with normal vectors parallel to the coordinate axes. The RVE is divided into 100 polyhedral grains with random size, shape and orientation. This cubic FEM model is a representation of a real grain structure and can be regarded as the product of the isotropic growth process from a spatial distribution of grain nuclei (Zhu et al., 2014). These grain nuclei are randomly generated one by one, and the subsequent ones are accepted only if they are located no nearer than an allowed distance from all others, thus the distance between two neighbor grains will not too close. The histogram of grain area ratio from one surface at  $x_1 = 0$  is exhibited in Fig. 5(a). In order to reflect the distribution of area ratios from different sections cut from the RVE, we take 30 sections from the RVE divided along the  $x_1$  direction. The respective histogram of grain area ratios is shown in Fig. 5(b), which is similar to Fig. 3 from the SEM metallographic image. The volume statistics reflects the grain structure different from the area statistics as shown in Fig. 5(c).

Each grain in the RVE has its individual orientation described by a unit vector which is generated by three randomly chosen values in the range from  $-1$  to  $1$ . The distribution of the orientations of all grains makes the RVE representing an approximately isotropic solid, which can be concluded from the  $\{100\}$  and  $\{111\}$  pole figures displayed in Fig. 6. The grains represent single crystals whose

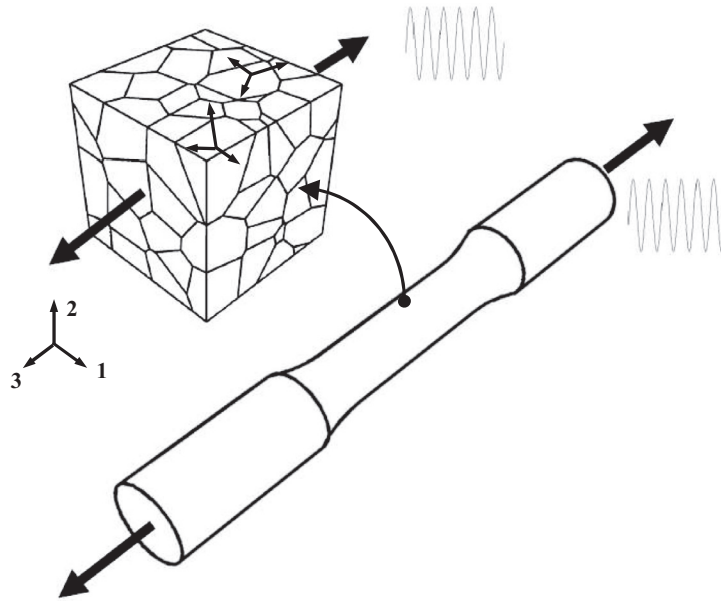


**Fig. 1.** A representative volume element consisting of a number of crystal grains which is taken from the specimen of a polycrystalline metal under cyclic loading.

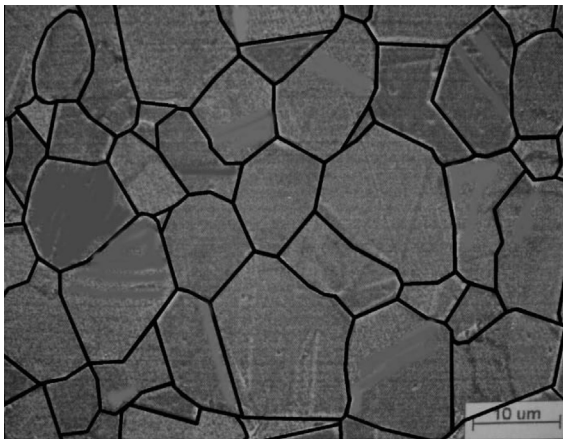


**Fig. 2.** The metallographic photo of GH4169 (cf. Li et al., 2013).

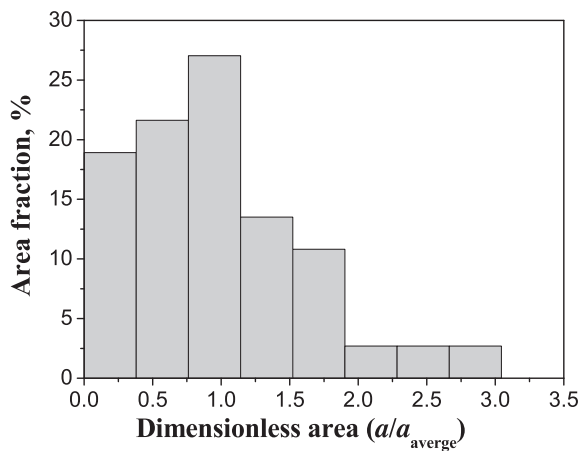


**Fig. 3.** The histogram of grain area for GH4169 according to Fig. 2.

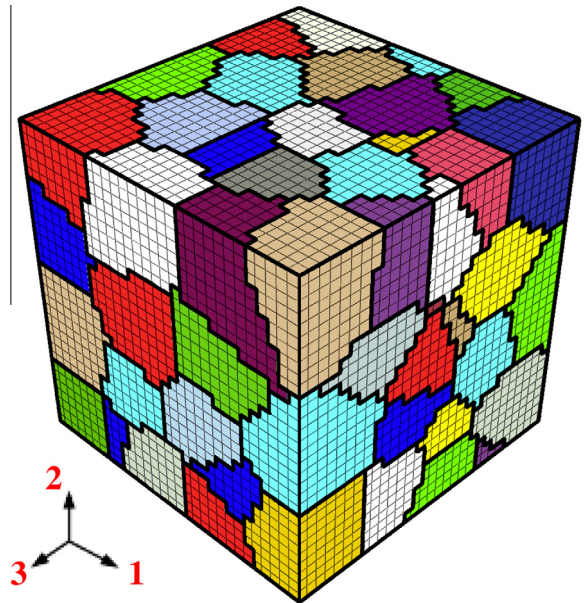


**Fig. 4.** The RVE model constructed by a Voronoi polycrystalline aggregation consisting of 27,000 eight-node hexahedral elements and 29,791 nodes.

anisotropic constitutive behavior is described by crystal plasticity. The macroscopic mechanical behavior of the homogenized polycrystalline material as well as the inhomogeneity of the deformation resulting from the micro-scale anisotropy and random microstructures can be numerically evaluated and the latter statistically described. The local stresses and strains for a material point in a grain are defined by the Cauchy stress tensor,  $\sigma$ , and the logarithmic strain tensor,  $\epsilon$ , respectively. The



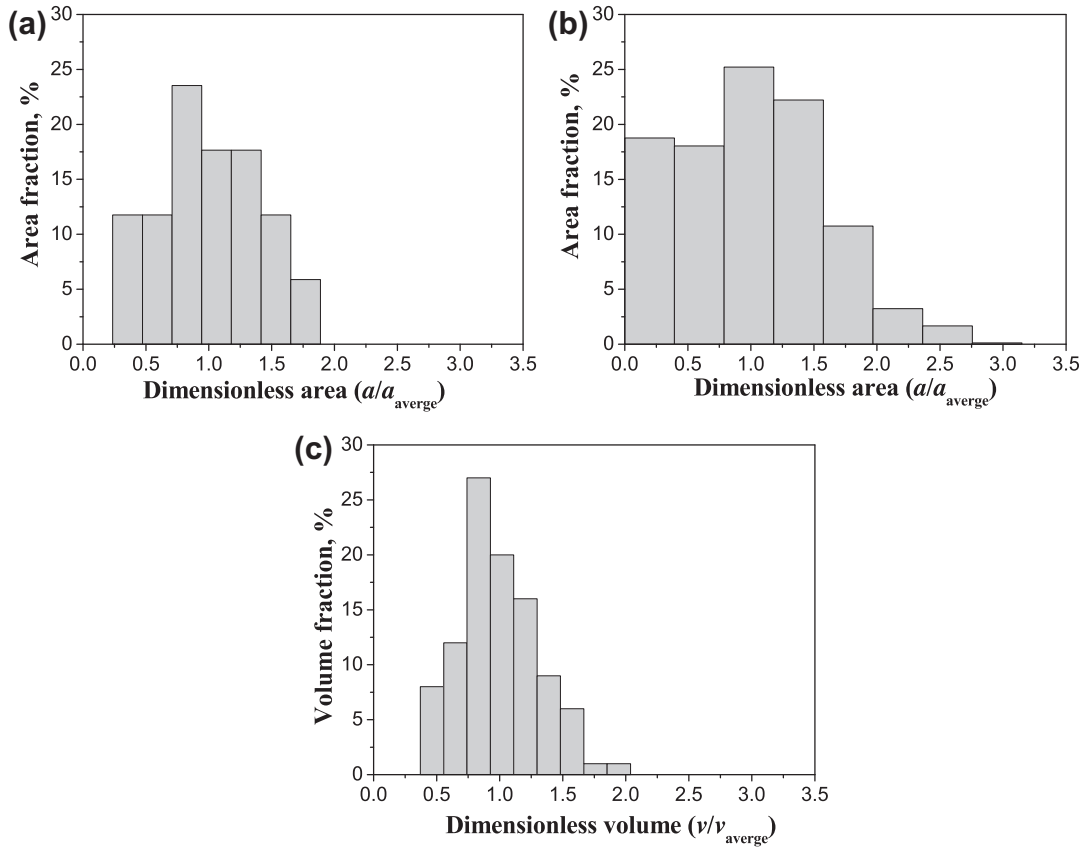


**Fig. 5.** The histograms of area and volume ratios for the model shown in Fig. 4; (a) grain area ratios from the view of the surface at  $x_1 = 0$ ; (b) grain area ratios as average of 30 equidistant sections along  $x_1$  direction; (c) volume ratios.

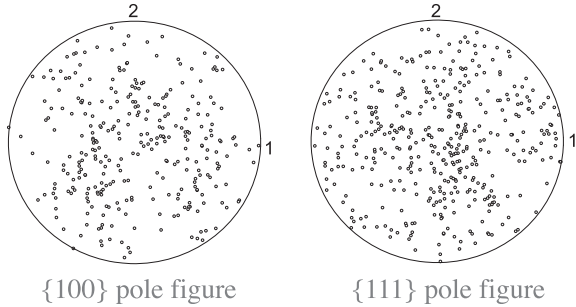


**Fig. 6.** The {100} and {111} pole figures of the material's initial texture for the present model.

homogenized overall ("macroscopic") Cauchy stresses and logarithmic strains are denoted by  $\Sigma$  and  $E$ .

Compatibility conditions for the macroscopic continuum require appropriate displacement constraints at the surfaces of the RVE. This can be realized by periodic boundary conditions or just by keeping all surfaces plane. Though the latter induces a higher constraint, it has been assumed in the present analyses as it is easier to establish. Finally, it turned out that there are no big differences in the results, anyway, see Fig. 28 below. The RVE is subjected to macroscopic uniform cyclic deformation as in the smooth

tensile specimen by prescribing a macroscopic longitudinal displacement,  $U_l = \bar{U}$ , at the upper surface whereas the lower surface is fixed. The lateral surfaces of the RVE are stress free, i.e.  $\Sigma_{ij} = 0$ ,  $i \neq j$ , and  $\sum_{il} = 0$  (the underlined subscripts indicate that no summation is executed),  $i \neq l$  and  $l = 3$ .

## 2.2. Constitutive equations of crystal plasticity with nonlinear kinematic hardening

The formulation of the constitution equations of crystal plasticity follows those by Hill and Rice (1972), Asaro and Rice (1977), Peirce et al. (1983), Needleman et al. (1985). Euler's velocity gradient tensor  $L$  is decomposed into an elastic part,  $L^*$ , and a plastic part,  $L^p$ ,

$$\begin{cases} L = \dot{F} \cdot F^{-1} = L^* + L^p, & L^* = \dot{F}^* \cdot F^{*-1}, \\ L^p = \dot{F}^* \cdot \dot{F}^p \cdot F^{p-1} \cdot F^{*-1} = \dot{F}^* \cdot \left( \sum_{\alpha=1}^n m^{(\alpha)} n^{(\alpha)} \dot{\gamma}^{(\alpha)} \right) \cdot F^{*-1}. \end{cases} \quad (1)$$

$F^*$  and  $F^p$  denote the elastic and the plastic part of the deformation gradient tensor  $F$ ;  $m^{(\alpha)}$  and  $n^{(\alpha)}$  are the unit vectors of the slip direction and the slip plane normal, respectively, for the  $\alpha$ -slip system with respect to the initial configuration (the assumed unloading configuration).

$\dot{\mathbf{F}}^*$  and  $\dot{\mathbf{F}}^p$  are the material derivatives of  $\mathbf{F}^*$  and  $\mathbf{F}^p$ ,  $\dot{\gamma}^{(\alpha)}$  is the resolved shear strain rate for the  $\alpha$ -slip system, and  $n$  is the number of slip systems.

For a material point in a crystal grain, the Euler's velocity gradient tensor  $\mathbf{L}$  can be decomposed into the symmetric part (the stretching tensor),  $\mathbf{D} = \text{sym}(\mathbf{L})$ , and the anti-symmetric part (the spin tensor),  $\mathbf{W} = \text{asym}(\mathbf{L})$ . Further, we write

$$\mathbf{D} = \mathbf{D}^* + \mathbf{D}^p, \quad \mathbf{W} = \mathbf{W}^* + \mathbf{W}^p \quad (2)$$

where  $\mathbf{D}^*$  and  $\mathbf{D}^p$  are, respectively, the elastic stretching tensor and the plastic stretching tensor;  $\mathbf{W}^p$  is the plastic spin tensor arising from slipping, and  $\mathbf{W}^*$  is the spin tensor arising from rigid body rotation and elastic distortion.

Hutchinson (1976) suggested an equation for the resolved shear strain rate, which describes the slip-system hardening without taking reversed loading into account. Considering the Bauschinger effect, Cailletaud (1992) introduced the back-stress and nonlinear kinematic hardening at the level of each slip system. In the present paper, we adopt the equation suggested by Feng et al. (2004):

$$\dot{\gamma}^{(\alpha)} = \dot{\gamma}_0 \text{sgn}(\tau^{(\alpha)} - x^{(\alpha)}) \left| \frac{\tau^{(\alpha)} - x^{(\alpha)}}{g^{(\alpha)}} \right|^k \quad (3)$$

where  $\tau^{(\alpha)}$  and  $x^{(\alpha)}$  are the resolved shear stress and back-stress on the  $\alpha$ -slip system, respectively;  $\dot{\gamma}_0$  denotes the reference shear rate, taken as a constant for all the slip systems;  $k$  denotes the rate sensitivity parameter. Furthermore,  $g^{(\alpha)}$  defines the scalar function describing the dimension of the elasticity domain for  $\alpha$ -slip system; its evolution is as follows (Pan and Rice, 1983):

$$\dot{g}^{(\alpha)}(\gamma) = \sum_{\beta}^n h_{\alpha\beta}(\gamma) |\dot{\gamma}^{(\beta)}|, \quad \gamma = \int \sum_{\beta}^n |d\gamma^{(\beta)}| \quad (4)$$

where  $h_{\alpha\beta}(\gamma)$  are the slip-plane hardening moduli. Further, Hutchinson (1970) proposed that

$$h_{\alpha\beta}(\gamma) = h(\gamma)[q + (1 - q)\delta_{\alpha\beta}], \quad (5)$$

where  $q$  is a constant, and Chang and Asaro (1981) suggested that

$$h(\gamma) = h_0 \sec h^2 \left( \frac{h_0 \gamma}{\tau_s - \tau_0} \right), \quad (6)$$

where  $h_0$  is the initial hardening rate,  $\tau_0$  is the critical resolved shear stress, and  $\tau_s$  is the saturation value. These parameters are regarded as material constants.

The evolution of back-stresses,  $x^{(\alpha)}$ , is introduced as (Zhang et al., 2011):

$$\dot{x}^{(\alpha)} = a\dot{\gamma}^{(\alpha)} - c \{1 - e_1[1 - \exp(-e_2\gamma)]\} x^{(\alpha)} |\dot{\gamma}^{(\alpha)}| - p x^{(\alpha)} \quad (7)$$

where  $a$ ,  $c$ ,  $e_1$ ,  $e_2$  and  $p$  are material constants. This formulation includes a strain hardening term, a dynamic recovery term, and a static recovery term. The identification of material constants in Eqs. (3), (5)–(7) is based on cyclic tests combined with numerical simulations.

Assuming that the elastic deformation is small, the constitutive relation can be expressed as:

$$\dot{\boldsymbol{\sigma}}^J = \overset{<4>}{\mathbf{C}} : \mathbf{D}^* = \overset{<4>}{\mathbf{C}} : (\mathbf{D} - \mathbf{D}^p) \quad (8)$$

where  $\dot{\boldsymbol{\sigma}}^J$  is the Jaumann rate of Cauchy stress,  $\overset{<4>}{\mathbf{C}}$  is the fourth-order tensor of the tangent elasticity with respect to the global coordinate axes. During the calculation, the global coordinate system is fixed, while the crystal coordinate axes for every individual grain are rotated along with the changing configuration which is determined according to the lattice rotation.

Therefore, the incremental change of the Cauchy stress tensor can be calculated as follows:

$${}^{t+\Delta t}\boldsymbol{\sigma} = {}^t\boldsymbol{\sigma}|_{t+\Delta t} + \Delta\boldsymbol{\sigma}^J, \text{ or } {}^{t+\Delta t}\boldsymbol{\sigma} = {}^t\boldsymbol{\sigma}|_{t+\Delta t} + \overset{<4>}{\mathbf{C}} : (\Delta\boldsymbol{\varepsilon} - \Delta\boldsymbol{\varepsilon}^p) \quad (9)$$

where the increments  $\Delta\boldsymbol{\sigma}^J$ ,  $\Delta\boldsymbol{\varepsilon}$  and  $\Delta\boldsymbol{\varepsilon}^p$  are determined by integrating the corresponding rates tensor  $\dot{\boldsymbol{\sigma}}^J$ ,  $\mathbf{D}$  and  $\mathbf{D}^p$ .

For details of the numerical implementation as user-supplied subroutine UMAT in the FE code ABAQUS see Zhang et al. (2013).

### 2.3. Parameter identification and validation of the constitutive model

The chemical composition of the alloy GH4169 is shown in Table 1 and the stable cyclic stress–strain curve for GH4169 at a temperature of 650 °C is exhibited in Fig. 7 (cf. Wu et al., 2008). Because no creep deformation has been observed for this material, creep is ignored in our analysis.

The cyclic stress–strain curve in Fig. 7 is determined by the loci of the stabilized hysteresis loop peaks at various strain amplitudes obtained from the cyclic experiments, which can be represented by a fitting equation  $\varepsilon = \frac{\sigma}{E} + \left(\frac{\sigma}{K'}\right)^{1/n'}$ , with  $E = 150500$  MPa,  $K' = 1412$  MPa,  $n' = 0.096$  (cf. Wu et al., 2008). Furthermore, the stable hysteresis loops are fitted by the approximation  $\frac{\Delta\varepsilon}{2} = \frac{\Delta\sigma}{2E} + \left(\frac{\Delta\sigma}{2K'}\right)^{1/n'}$ . The material has Masing behavior (Masing, 1926), since there is a stable hysteresis loop. The experimental hysteresis loops can be used as target solutions to conduct the parameter identification. The model for describing the elastic and plastic behavior of a single crystal contains 14 parameters. In addition to the

**Table 1**  
Chemical composition of the GH4169 superalloy (wt%).

C	Cr	Mu	Nb + Ta	Ni	Fe	Al	Ti
0.015–0.08	17.0–21.0	2.80–3.80	4.75–5.50	50.0–55.0	Rest	0.30–0.70	0.75–1.15
Si	Mn	Co	Cu	P	S	B	
≤0.35	≤0.35	≤1.00	≤0.30	≤0.015	≤0.015	≤0.006	

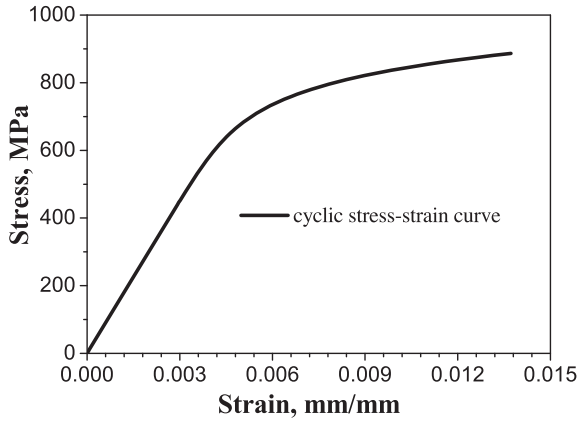


Fig. 7. The experimental stable cyclic stress–strain curve for GH4169 at temperature 650 °C (cf. Wu et al., 2008).

three elastic constants  $C_{11}$ ,  $C_{12}$  and  $C_{44}$ , eleven parameters remain for plasticity based on slipping of fcc slip-system, which are  $\tau_0$ ,  $\tau_s$ ,  $h_0$ ,  $a$ ,  $c$ ,  $p$ ,  $e_1$ ,  $e_2$ ,  $\dot{\gamma}_0$ ,  $q$  and  $k$ . They have certain physical meanings:  $\tau_0$  and  $\tau_s$  are the critical resolved shear stress and the saturation value, respectively, which are related to the initial yield strength or the elastic range between the points of unloading and re-yielding in the stress–strain hysteresis loop;  $a$ ,  $c$  and  $p$  describe strain hardening in a loop;  $e_1$  and  $e_2$  are used to describe cyclic hardening after some ten cycles, if existent;  $\dot{\gamma}_0$  is a reference strain rate, and  $k$  quantifies the rate sensitivity of the material;  $q$  is a parameter to consider the interaction between slip-systems. Therefore, parameter identification can be conducted sequentially, referring to separate characteristics of experimental stress–strain loops.

Parameter identification requires an experimental reference solution, a criterion for quantifying the difference between the numerical results and the test data, and an algorithm for parameter variation. The coincidence between numerical and test results can be rated optically or quantified by some “objective” or target function which depends on the user’s definition. The outcome will obviously be affected by this choice, and depending on details of the target function like number of points, optical coincidence may even result in higher accuracy. Numerous algorithms exist for varying the parameters, trial and error, Monte Carlo, mathematical optimization, evolution strategies, neural networks, having their individual advantages and limitations (Brocks and Steglich, 2007), which cannot be discussed in detail, here. A “trial-and-error” procedure is generally time consuming but its results with respect to parameter identification are not as “improper” as the term might indicate. Systematic variations of parameters require a phenomenological interpretation and an understanding of the respective effects on the mechanical response of the structure. This calls for expert knowledge,

and the outcome is all the more successful and the time spent so much less the more experienced the user is.

Considering optical congruence of numerical and experimental results and the physical background of individual parameters, the constitutive parameters are determined by trial-and-error according to the following procedure. In the first step, the parameters  $\tau_0$ ,  $p$ ,  $e_1$ ,  $e_2$ ,  $\dot{\gamma}_0$ ,  $q$  and  $k$  can be set without calculation:  $p = 0$ , since creep during cyclic loading is ignored;  $e_1 = e_2 = 0$ , as cyclic hardening is not necessary to be considered for the stable cyclic process;  $q = 1$ , because the hardening from slipping is considered the same for all slip-system;  $\dot{\gamma}_0 = 0.01$  which is proper for the considered low loading rate;  $k = 150$ , since the rate sensitivity of the material is very small. In the second step,  $\tau_0$ ,  $\tau_s$ ,  $h_0$  which depend on the elastic range of the experimental hysteresis loops are determined by simulation. In this step, the parameters  $a$  and  $c$  are given a rough initial value, for example several GPa for  $a$  and one tenth for  $c$ , since  $\tau_0$ ,  $\tau_s$ ,  $h_0$  characterize isotropic hardening and are not sensitive to  $a$  and  $c$ , which are related to the evolution of the backstress in kinematic hardening. In the third step, the parameters  $a$  and  $c$  are identified by calculations of cyclic loading to simulate the experimental hysteresis loop. The parameters  $a$  and  $c$  have specific meanings in the hysteresis loop:  $a$  governs the initial hardening ratio for slipping and  $c$  is related to softening.

The identification of model parameters for crystal plasticity is performed by calibration using the experimental data of hysteresis loops from cyclic tests, which are fitted by the approximation  $\frac{\Delta\sigma}{2} = \frac{\Delta\sigma}{2E} + \left(\frac{\Delta\sigma}{2K'}\right)^{1/n'}$  (see previous page denoting the parameters). All the model parameters of crystal plasticity as determined by this procedure are listed in Table 2.

In order to verify the parameter identification, referring to the work by Sweeney et al. (2014b), an error function is defined,

$$F_k = \sqrt{\frac{1}{n} \sum_i^n (\Sigma_i^{\text{exp}(k)} - \Sigma_i^{\text{sim}(k)})^2} \quad k = 1, 2, \dots, 10 \quad (10)$$

where  $k$  is a number denoting the ten different strain amplitudes 0.0045, 0.005, 0.006, 0.007, 0.008, 0.009, 0.010, 0.011, 0.012 and 0.013, respectively;  $n$  is the number of points of the stable hysteresis loop;  $\Sigma_i^{\text{exp}(k)}$  and  $\Sigma_i^{\text{sim}(k)}$  are the stresses, respectively, measured in experiment and calculated in simulation for  $k$ th strain amplitude and  $i$ th point. The errors of the model for different strain amplitudes are listed in Table 3, in which the maximum of  $F_k$  is less than 1.75 MPa, which is regarded as acceptable. Fig. 8 shows the comparison of the experimental cyclic stress strain curve with hysteresis loops calculated for strain amplitudes 0.005, 0.009 and 0.012. All hysteresis loops simulated by applying the RVE are shown in Fig. 9.

Table 2

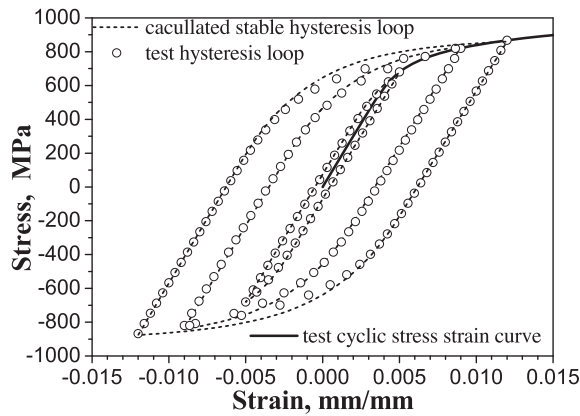
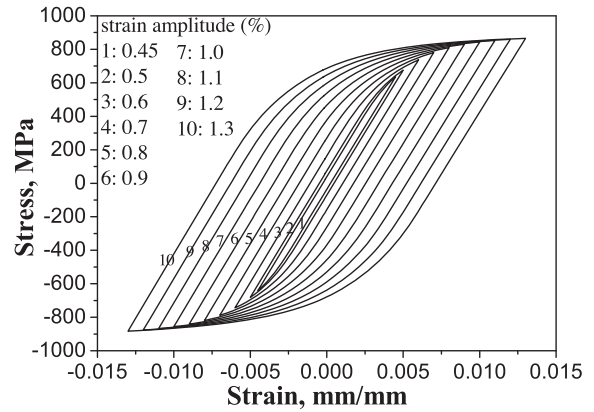
Crystal elastic constants and plasticity parameters of the GH4169 superalloy.

Elastic constants			Material parameters of the crystal viscoplastic model (under 650 °C)										
$C_{11}$ GPa	$C_{12}$ GPa	$C_{44}$ GPa	$\tau_0$ MPa	$\tau_s$ MPa	$h_0$ MPa	$a$ GPa	$c$ GPa	$p$ s <sup>-1</sup>	$e_1$	$e_2$	$\dot{\gamma}_0$ s <sup>-1</sup>	$q$	$k$
206.7	137.98	73.65	260	265	80	35	0.43	0	0	0	$1 \times 10^{-3}$	1	150

**Table 3**

Error between model calculation and experimental data for hysteresis loops.

Number $k$	1	2	3	4	5	6	7	8	9	10
Strain amplitude $\frac{1}{2}\Delta\epsilon_t$ (%)	0.45	0.5	0.6	0.7	0.8	0.9	1.0	1.1	1.2	1.3
Error ( $F_k \leq$ )	0.26	0.30	0.47	0.92	1.35	1.61	1.73	1.75	1.71	1.67

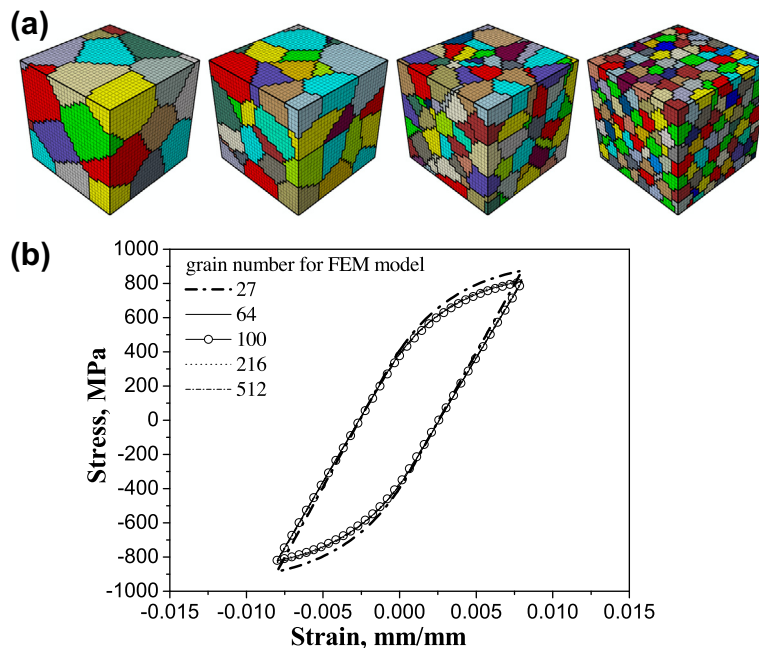
**Fig. 8.** The comparison of the experimental cyclic stress strain curves with hysteresis loops calculated for strain amplitudes of 0.005, 0.009 and 0.012.**Fig. 9.** All 10 hysteresis loops at various strain amplitudes obtained by simulations.

#### 2.4. Validation of the RVE

A further validation of the RVE is given in the following with respect to the aspects (i) whether it reflects the behavior of a polycrystal, and (ii) whether the model consists of enough grains and finite elements. As the individual grain is anisotropic enough grains are required, so

that the RVE can simulate the homogenized behavior macroscopically. The number of elements is significant for the model in order to obtain a numerically convergent solution.

Fig. 10(a) shows 4 models with the same number of 27,000 elements but containing 27, 64, 216 and 512 grains. Fig. 10(b) shows the respective hysteresis loops at a strain amplitude of 0.8%. The differences in macro hysteresis loop

**Fig. 10.** (a) 4 models with same number of 27,000 elements but containing 27, 64, 216 and 512 grains; (b) hysteresis loops simulated at a strain amplitude of 0.8% compared with that by the model containing 100 grains.



are marginal, and the curves are nearly the same for the models containing 64, 100, 216 and 512 grains.

Fig. 11(a) displays 2 models containing the same number of 100 grains but consisting of 8,000 and 64,000 elements, and Fig. 11(b) shows the comparison of the respective hysteresis loops, at a strain amplitude of 0.8%. The difference in macroscopic hysteresis loop is very small. The FE discretization affects the shape of the grain boundaries: the fewer elements the coarser are the grain boundaries, which may have an impact on additional inhomogeneities of the strain fields. The calculations using the above FE models of Fig. 11(a) can reflect the respective influence on inhomogeneous strain fields. The standard deviations of strains in loading direction with number of cycles for the three models are shown in Fig. 11(c), from

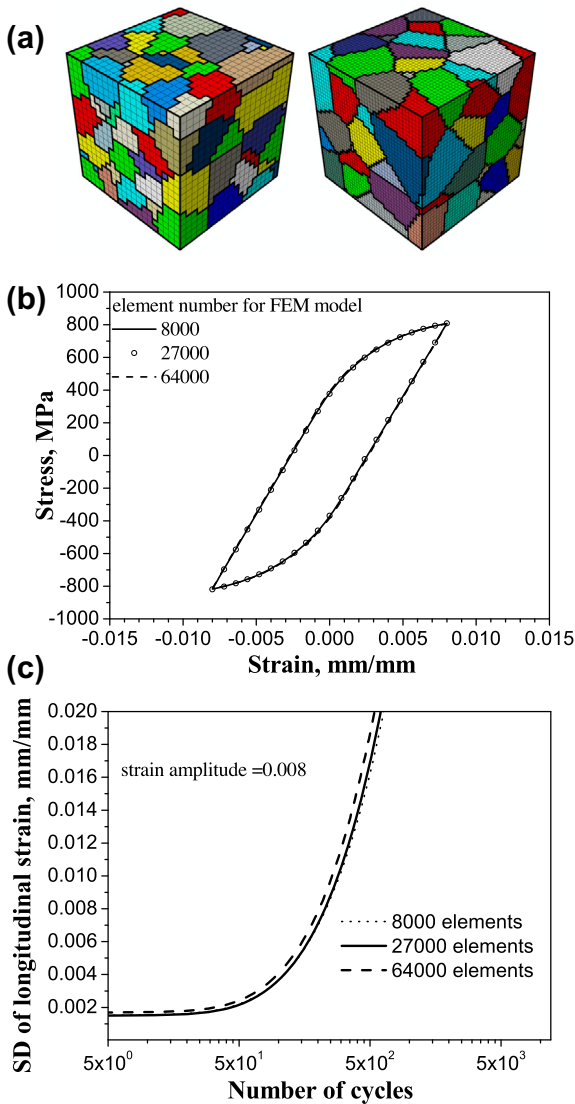


**Fig. 11.** (a) Two models containing the same number of 100 grains with 8,000 and 64,000 elements, respectively; (b) hysteresis loops simulated under cyclic loading at a strain amplitude of 0.8%; (c) standard deviation of longitudinal strain vs number of cycles for varying number of elements.

which one can find that the difference not considerable. Here, we need point out that the abscissa is log scaled which is convenient to display a range of several orders of magnitude of load cycles.

The following analysis is used to discuss the influence of mesh refinement on the macro response and strain inhomogeneities at grain level. Two bicrystal models with coarse and smooth grain boundary, respectively, are introduced, see Fig. 12(a). Two conditions for orientations are considered: (i) [001] for grain 1 and [111] for grain 2; (ii) [001] for grain 1 and, [110] for grain 2. The macroscopic hysteresis loops for the models are shown in Fig. 12(b), and the standard deviations of strains in loading direction with number of cycles are exhibited in Fig. 12(c). The differences between the models with coarse or smooth boundary are actually so small that they can be ignored.

Hence, according to the analyses above, it can be concluded that the model containing 100 grains and 27,000 elements represents a valid RVE to investigate the inhomogeneous strain under cyclic loading.

## 2.5. Statistical analysis of the RVE

In order to discuss the relationship of inhomogeneous strain and fatigue life for a polycrystal, a methodology was proposed by Zhang et al. (2013). In this methodology, the inhomogeneous micro stresses and strains of a Voronoi polycrystalline aggregation under cyclic loading are described by statistical parameters. The stresses and strains in the RVE at the grain level during the deformation processes with various macroscopic strain amplitudes are tracked and their mean values and corresponding standard deviations are calculated:

$$\begin{aligned} \bar{\sigma}_{ij} &= \sum_{k=1}^{n_{RVE}} (\sigma_{ij})_k p_k, & \bar{\epsilon}_{ij} &= \sum_{k=1}^{n_{RVE}} (\epsilon_{ij})_k p_k, \\ \hat{\sigma}_{ij} &= \sqrt{\sum_{k=1}^{n_{RVE}} (\sigma_{ij})_k^2 p_k - \bar{\sigma}_{ij}^2}, & \hat{\epsilon}_{ij} &= \sqrt{\sum_{k=1}^{n_{RVE}} (\epsilon_{ij})_k^2 p_k - \bar{\epsilon}_{ij}^2}, \end{aligned} \quad (11)$$

where  $n_{RVE}$  is the total number of finite elements in the RVE;  $\sigma_{ij}$  and  $\epsilon_{ij}$  are the components of the local Cauchy stress tensor and the logarithmic strain tensor, respectively; the subscript  $k$  denotes the  $k$ th element;  $p_k = \Delta V_k / V$ , with  $\Delta V_k$  denoting the volume of  $k$ th element and  $V$  the total volume of the RVE.

The higher the standard deviation is, the larger is the data scatter within the RVE.

## 2.6. A criterion for the fatigue failure of a polycrystalline material

A classical methodology to assess fatigue life of a material undergoing cyclic loading with specified strain amplitude usually adopts some function:

$$f(\Delta\epsilon, N_f) = C, \quad (12)$$

where  $\Delta\epsilon$  is the strain amplitude and  $N_f$  the number of loading cycles to fatigue failure, and  $C$  denotes the fatigue strength of the material. Provided that the two or more parameters have been determined by fatigue experiments

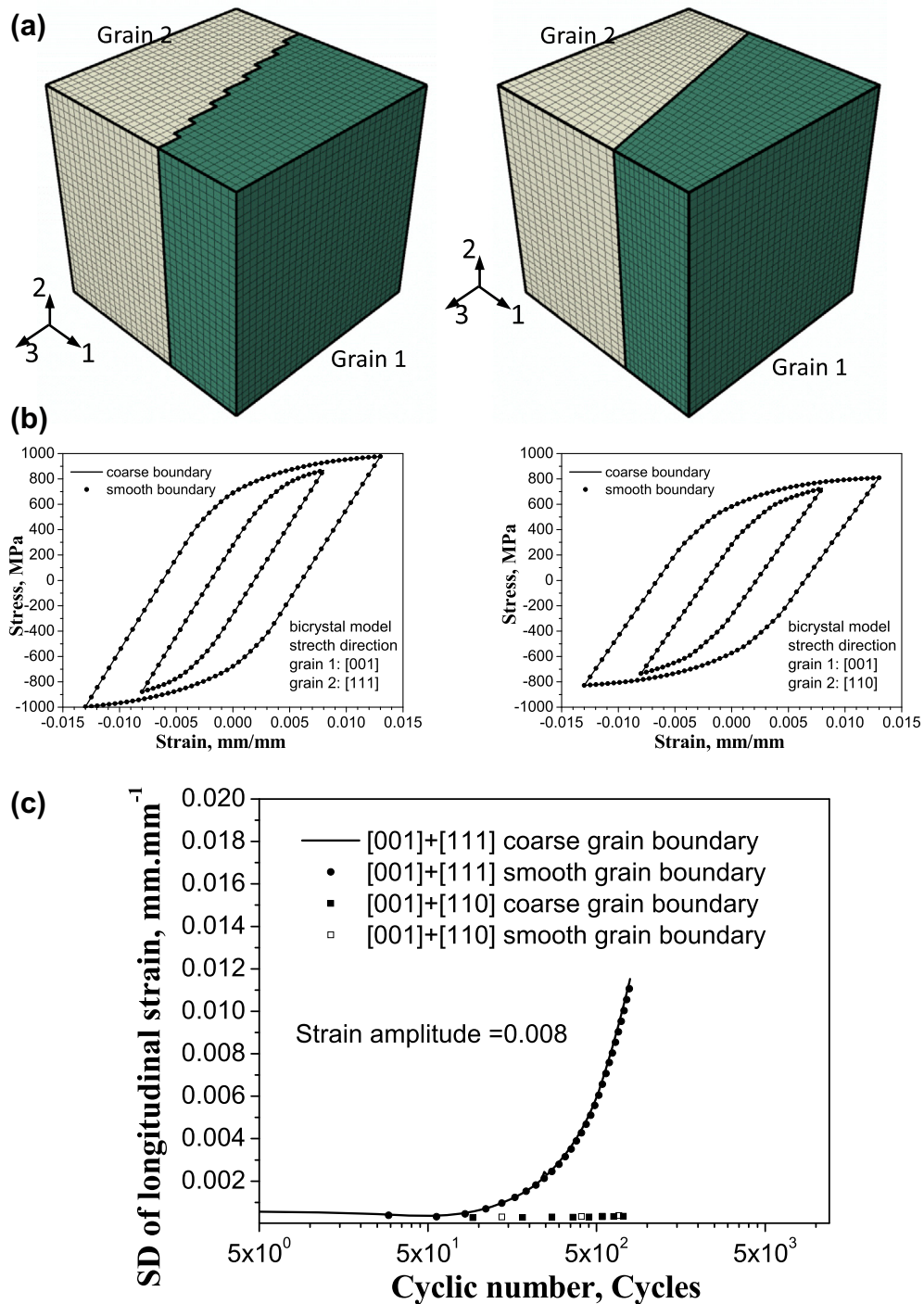


**Fig. 12.** (a) FEM models of bicrystals; (b) hysteresis loops of the models containing two single crystal grains with different orientations; (c) standard deviations of strain in the loading direction with cycling for different bicrystal models.

on a number of specimens, this equation can be applied to assess the fatigue life of components. The classical models of fatigue life prediction are phenomenological, completely established on the basis of macro experiments, and usually have two or more parameters to be determined by fatigue tests. Since fatigue of metals involves very complicated

processes and factors whereas the fatigue experiments to calibrate the model parameters are performed under very simple loading conditions, only, it is fairly difficult for a phenomenological macro model to predict the fatigue life of a material under actual loading conditions. In order to establish a more physical model, it is necessary to consider

both the deformation mechanisms at the micro-scale and the corresponding macroscopic responses.

Numerical simulations under symmetrical strain controlled cyclic loading of the above RVE indicate that the standard deviations of the longitudinal strains at the tensile peak increases with increasing number of cycles (Zhang et al., 2013). These results give reason to the assumption that a limit value of the strain standard deviation can be regarded as a material constant,  $\hat{\epsilon}_{fatigue}$ , for low-cycle fatigue failure

$$\hat{\epsilon}_{ll} = \hat{\epsilon}_{fatigue} \quad (13)$$

This criterion implies the following. (a) The strain components along the loading direction grow although the macro strain amplitude is kept unchanged, and their scatter increases due to the evolution of inhomogeneity of the material. (b) The standard deviation of the microscopic strains will reach a high values but has a limit, and fatigue failure will occur as this limiting value is reached. (c) This limit is approximately a material constant under cyclic loading with various macro strain amplitudes.

Only one parameter is needed for the above method to assess fatigue failure. If we define a series of values for the limit value,  $\hat{\epsilon}_{fatigue}$ , in a parameter study, a corresponding family of fatigue life curves can be calculated in dependence on the global strain amplitude, and the actual limit value can be determined by comparison with fatigue test results.

### 3. Low-cycle fatigue simulations

#### 3.1. Simulation of tensile-compressive cyclic loading at various strain amplitudes

Numerical calculations tracking the cycles for the RVE with ten strain amplitude levels  $\frac{1}{2}\Delta E_t$  (0.45%, 0.5%, 0.6%, 0.7%, 0.8%, 0.9%, 1.0%, 1.1%, 1.2% and 1.3%) are performed step by step, respectively; each step consists of 1000 cycles including 200,000 increments (i.e., each cycle consists of 200 increments). The aim of the calculation is to observe the variance of the strains in the RVE from which the local strain reaching higher levels than the average can be evaluated (see Eq. (11)), whereas the average value is controlled by the macro loading.

The calculation for the entire cyclic process requires a large number of steps. The computational effort is considerable. In particular, for the case with small strain amplitude, the number of increments can reach a very high value. For example, when  $\frac{1}{2}\Delta E_t = 0.45\%$ , the total number of increments is more than 1,600,000. To complete the demanding calculations the “restart write” function of the ABAQUS software is employed to prepare alternate restart files at intervals of every 6000 increments.

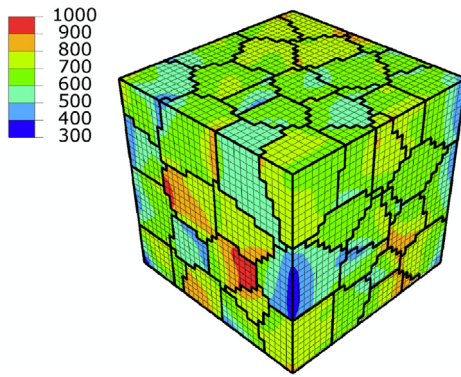
There are some clear advantages to adopt the crystal viscoplasticity model associated with a RVE to simulate the material low-cycle process. Not only the apparent responses of the metallic material under cyclic loading can be simulated, but also the distribution of the inhomogeneous internal stresses and strains can be computed, including the two statistical parameters of average and

standard deviation (root mean square deviation) and their evolution with cycles. Therefore, we can compute the mesoscopic hysteresis loops  $\Sigma \sim E$  (or  $\Sigma_{ll} \sim E_{ll}$ , as above, with the direction of the  $l$ -axis set as the macro uniaxial loading direction, where the underline under the second subscript  $l$  means that no summation for the tensor component is executed) for various strain amplitudes,  $\frac{1}{2}\Delta E_t$ , of 0.45%, 0.5%, 0.6%, 0.7%, 0.8%, 0.9%, 1.0%, 1.1%, 1.2% and 1.3%, in the stabilized state. These numerical simulations track the tested cyclic responses of macro stress-strain curves just like performing the tests. However, different from common calculations, they provide the evolution of the stresses, strains and the microstructure.

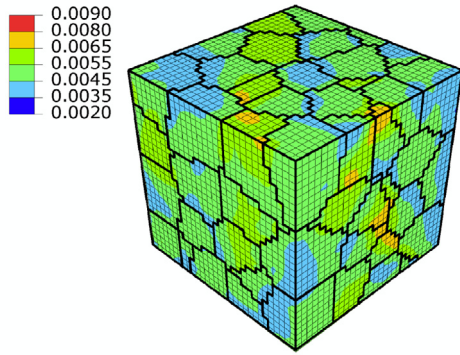
#### 3.2. Evolution of inhomogeneous stress and strain fields

Although a uniform cyclic strain is applied to the RVE at the macro-scale, all grains are strained non-uniformly at the microscale due to the heterogeneous microstructure, the anisotropic mechanical behavior of grain, and the strong intergranular constraint. Fig. 13 shows the distributions of longitudinal stress and strain components in the RVE by contours, corresponding to the cyclic strain amplitude of 0.005 as well as the tension peaks of the 3rd cycle and the 3000th cycle. From the figure and the data in the legend box, it is observed that the variances of longitudinal stress and strain between the 3rd cycle and the 3000th cycle are very large, particularly for the longitudinal strain. This result can also be represented by histograms as in Fig. 14, where the distributions of longitudinal stress and strain components  $\sigma_{ll}$  and  $\epsilon_{ll}$  are clearly displayed. It reveals that the strain range has ten-times increased between the 3rd and the 3000th cycle. Moreover, the distributions of the longitudinal stress  $\sigma_{ll}$  and strain  $\epsilon_{ll}$  follow the Gaussian-like law. Therefore, they can be described by their mean values  $\bar{\sigma}_{ll}$  and  $\bar{\epsilon}_{ll}$ , and their standard deviations  $\hat{\sigma}_{ll}$  and  $\hat{\epsilon}_{ll}$ . The mean values reflect the responses of the material at the macroscale of the RVE, and the standard deviations depict the degree of fluctuation of stresses or strains within the material at grain-level. Since the distribution variance for the longitudinal stress in the same process is much smaller than that for strain, the longitudinal strain standard deviation is taken as a variable to assess the fatigue life (see Eq. (13)). Accordingly, the statistical analyses are carried out for the simulations under different cyclic strain amplitudes as aforementioned. Similar conclusions can be drawn as above; i.e., all the local strain ranges in the RVE have ten-fold increased between the initial cycle to the cycle near fatigue end, and all distributions for the longitudinal stress and strain components,  $\sigma_{ll}$  and  $\epsilon_{ll}$ , are Gaussian-like. Due to page limitations, respective results other than Figs. 13 and 14 are omitted here.

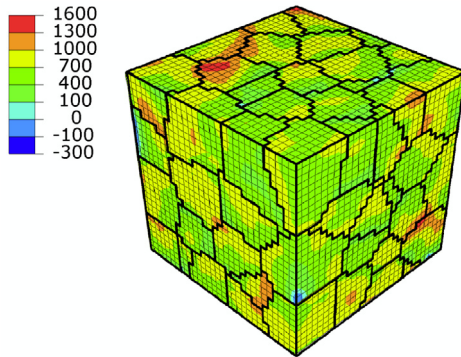
The external cyclic loading will give rise to the inhomogeneous evolution of the material microstructure due to repeated non-uniform plastic slip and the variance of stresses and strains in the material volume will increase. Whereas it is very difficult to experimentally measure this micro-processes in a material, the micro stresses and



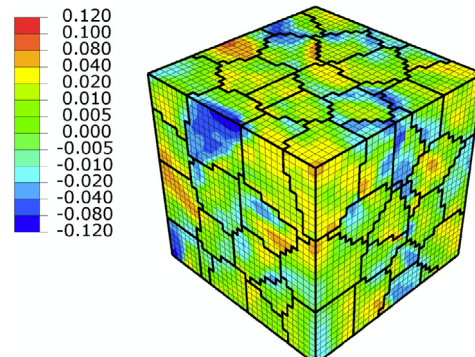
Longitudinal stress contours at the tension peak of the 3rd cycle, MPa



Longitudinal strain contours at the tension peak of the 3rd cycle, mm/mm

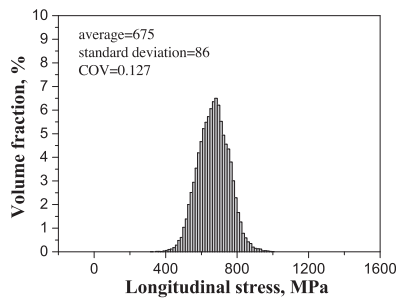


Longitudinal stress contours at the tension peak of the 3000th cycle, MPa

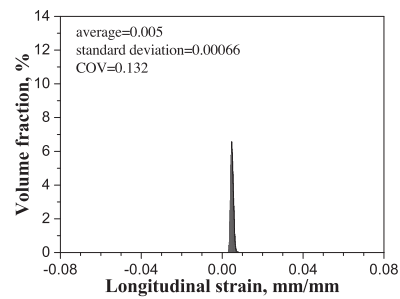


Longitudinal strain contours at the tension peak of the 3000th cycle, mm/mm

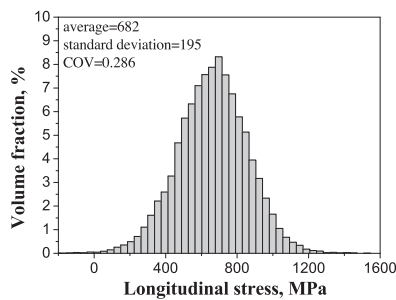
**Fig. 13.** The iso-contours of longitudinal stress and strain components for a strain amplitude of 0.005 at the tension peaks of the 3rd cycle and the 3000th cycle.



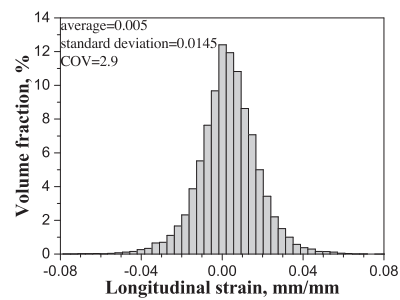
Longitudinal stress distribution for the RVE at the tension peak of the 3rd cycle



Longitudinal strain distribution for the RVE at the tension peak of the 3rd cycle



Longitudinal stress distribution for the RVE at the tension peak of the 3000th cycle



Longitudinal strain distribution for the RVE at the tension peak of the 3000th cycle

**Fig. 14.** The statistical distributions of the longitudinal stress and strain components,  $\sigma_{II}$  and  $\varepsilon_{II}$ , for the RVE at the tension peaks of the 3rd and 3000th cycle.



strains and plastic slipping mechanism in crystal grains can be obtained from the simulations.

To discuss the role of the inhomogeneous deformation in fatigue, we first take the results of the simulation to obtain the statistical characterization and evolution of the longitudinal strain (cf. Zhang et al., 2011; Zhang et al., 2013), and then perform the analysis of the fatigue life for GH4169 by using the criterion of Eq. (13). Fig. 15 displays the evolution and variation of the standard deviation  $\hat{\varepsilon}_{II}$ , for the micro longitudinal strain in the RVE under different strain amplitudes at the tension peak with cycle number. It shows that  $\hat{\varepsilon}_{II}$  at the tension peak monotonically increases with the cycle number and indicates that the accumulation of the plastic deformation in the RVE becomes increasingly inhomogeneous. This is consistent with results presented in the literature (Zhang et al., 2013), in which the target material is a copper. Here, we need point out that, (1) the abscissa in Fig. 15 is log scaled for a clear representation of the curves according to common practice; (2) the curves would appear approximately linear after a certain number of cycles if displayed on a linearly scaled axis.

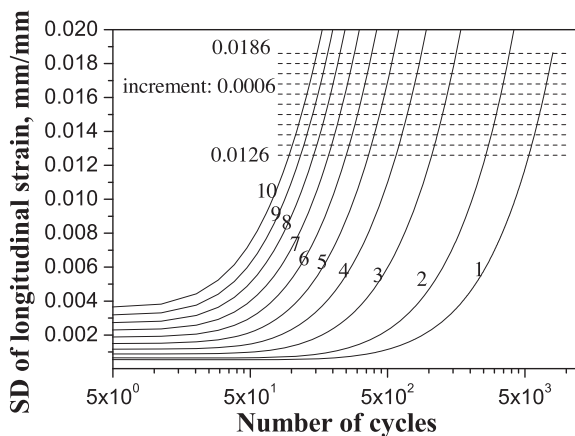


**Fig. 15.** The evolution and variation of the standard deviation (SD)  $\hat{\varepsilon}_{II}$ , of the micro longitudinal strain under different strain amplitudes at the tension peak with number of cycles. The horizontal lines indicate various limit value of the statistical standard deviation.

### 3.3. Low-cycle fatigue life prediction based on strain inhomogeneity and its verification

The lives of most materials tested under uniaxial cyclic loading are found to be dominated by crack initiation, which can be called initiation controlled fatigue. This is adopted here, too.

Local failure will occur in the material once the micro tensile strain reaches certain limits which the material cannot bear. According to Eq. (13), fatigue failure takes place when the standard deviation of the strains  $\varepsilon_{II}$  reaches a critical value.

It is necessary to point out that Eq. (13) as a criterion to judge fatigue rupture is only an assumption. We need to provide more evidence to confirm it. Generally, there are many factors influencing the fatigue failure of a material. Nevertheless, for the most-studied uniaxial strain controlled symmetric tension–compression fatigue, the loading condition is fairly simple and we can assume that the critical value of strain standard deviation is a constant, regardless of the applied strain amplitude. Other factors such as loading path and stress triaxialities are ignored temporarily.

Let us set a series of limiting values of the statistical standard deviation  $\hat{\varepsilon}_{II}$ , denoted as  $\hat{\varepsilon}_{II}^*$  as displayed by horizontal lines in Fig. 15, where, the number of limiting lines is 11 and the specified data for  $\hat{\varepsilon}_{II}^*$  range from 0.0126 to 0.0186 with increment 0.0006. These lines intersect with the curves of strain standard-deviation vs. cycle number, and the number of cycles for fatigue failure can be identified according to the assumed limit value of strain standard deviation. The respective data are listed in Table 4.

Subsequently, a family of curves for fatigue life can be plotted according to Table 4 as in Fig. 16. For comparison, the experimental fatigue life data of GH4169 at a temperature of 650 °C for strain amplitudes,  $\frac{1}{2}\Delta E_t$ , of 0.45%, 0.6%, 0.8%, 0.9, 1.0% and 1.3%, which are obtained from the literature (Wu et al., 2008, page 511), are also included. We find that the fatigue life curve can be described by the function,  $f(\Delta E_t, N_f) = \hat{\varepsilon}_{II}^*$ , which resembles Eq. (12). However, the present result is obtained by simulations and based on Eq. (13) under the conditions that the

**Table 4**  
Fatigue life prediction for various critical values of strain standard deviation.

$\hat{\varepsilon}_{II}^* = \frac{1}{2}\Delta E_t$ (%)	.0126	.0132	.0138	.0144	.0150	.0156	.0162	.0168	.0174	.0180	.0186
$N_f$											
1.3	96	101	107	113	118	124	130	135	141	147	153
1.2	117	123	129	136	142	149	156	162	169	176	183
1.1	145	153	161	168	176	184	192	200	209	217	225
1.0	186	196	205	215	225	235	245	256	266	276	287
0.9	250	263	276	289	302	316	329	342	356	370	384
0.8	363	382	401	419	438	458	477	497	516	536	556
0.7	577	607	636	666	696	727	757	789	820	852	883
0.6	1050	1101	1153	1205	1257	1310	1363	1417	1471	1525	1580
0.5	2600	2723	2848	2972	3097	3222	3348	3475	3602	3731	3861
0.45	5351	5608	5866	6126	6387	6648	6910	7174	7438	7704	7973



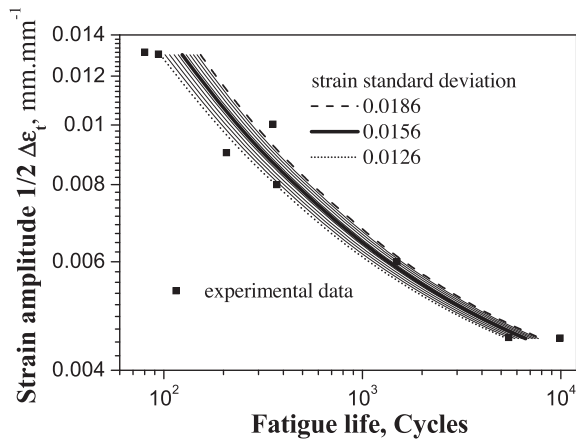


**Fig. 16.** Fatigue life curves of strain amplitude versus number of cycles for various limit values of the standard deviation of longitudinal strains according to Table 4 compared to experimental fatigue life data of GH4169 for strain amplitudes of 0.45%, 0.6%, 0.8%, 0.9, 1.0% and 1.3% at a temperature of 650 °C. The specified data for  $\hat{\epsilon}_{\text{eff}}$  is from 0.0126 to 0.0186 with increment 0.0006 (Wu et al., 2008, page 511).

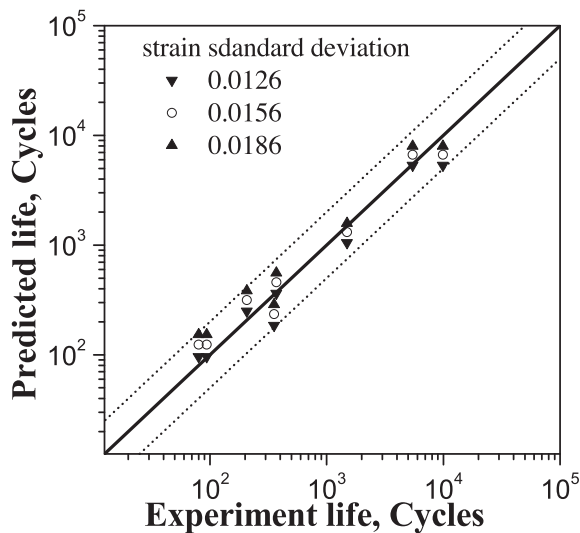


**Fig. 17.** Comparison of the predicted lives assessed according to the strain standard deviation limits 0.0186, 0.0156 and 0.0126, respectively, with the corresponding experimental fatigue lives, for strain amplitudes of  $\frac{1}{2} \Delta \epsilon_f$ : 0.45%, 0.6%, 0.8%, 0.9, 1.0% and 1.3%.

hysteresis loops and the grain structures of the material are known, without referring the material fatigue tests.

Comparing the calculated results with experimental data indicate that the predicted fatigue life curves are reasonable. The predicted curves render the estimated fatigue life by various limit values of the standard deviation of longitudinal strain, in which the maximum, median and minimum for the limits are 0.0186, 0.0156 and 0.0126, respectively. Taking these three curves, the comparisons of the experimental fatigue lives with the predictions made by the present calculations can be exhibited in Fig. 17. In this figure, the abscissa denotes the experimental fatigue

life, and the ordinate the predicted fatigue life. The thick solid diagonal line indicates a perfect prediction, and the two dotted lines represent the factor-of-two boundaries. Obviously, the predictions of the models by maximum, middle and minimum limit values of the local longitudinal strain standard deviation are within the factor-of-two lines.

### 3.4. Further discussions on the fatigue criterion

For crack initiation controlled fatigue, different criteria were proposed by different consideration to fatigue mechanisms. Manonukul and Dunne (2004) proposed a fatigue crack initiation criterion based on a critical accumulated slip, and the accumulated slip can be estimated by the effective plastic strain,  $p$ . They found that the lives of the polycrystals for LCF and HCF can be described well by using crystal plasticity combined with this criterion. Guerchais et al., 2014 suggested the micro stress threshold might be better as a fatigue criterion for HCF. Sweeney et al., 2013 found that the effective plastic strain per cycle

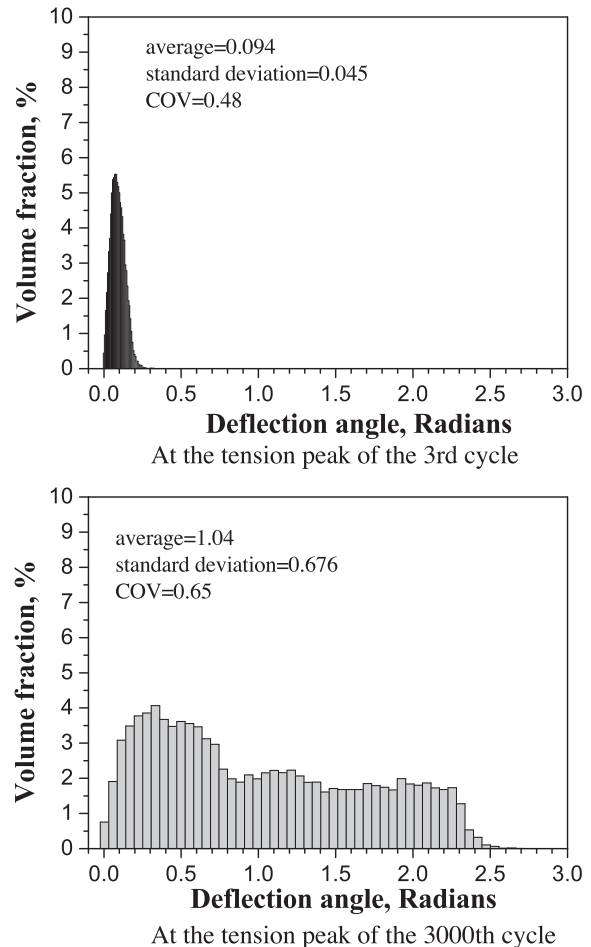


**Fig. 18.** The variance of the deflection of first principal direction with macro uniaxial loading direction calculated at the tension peaks of the 3rd cycle and the 3000th cycle under the condition with strain amplitude 0.005.

is a better indicator of fatigue crack nucleation than peak effective plastic strain by considering of the later changing in location. Sangid et al., 2011 proposed that the energy of the PSB can be calculated at both continuum and atomistic scale, and the stability of this energy with respect to dislocation motion can be taken as the failure criterion for fatigue crack initiation. By this approach, more aspects of material microstructures and their roles to fatigue failure can be considered.

In our approach, the standard deviation of strain in loading direction is found to increase with load cycles. Assuming that this parameter reaches a limit value when fatigue occurs and is constant for different strain amplitude can yield predictions which have good consistency with test results, see Figs. 16 and 17.

The investigations can be further extended on the average and maximum of principal strain, which both also increase with cycling. More details and numerical results are given below. Here, it is necessary to point out that particularly for multi-axial loading the maximum principal

strain would be appropriate. Because it is independent on the choice of global coordinates.

For a homogeneous isotropic material under uniaxial loading, the strains in the material are uniform and are the same as the corresponding principal strains, on the conditions that the directions of coordinate axes for defining the strains are chosen as the same as the principal directions. But for an inhomogeneous material such as the polycrystal presented in this paper, the conclusion above is incorrect because the inhomogeneity gives rise to the deflection of principal directions. According to the definition  $\varepsilon_1 \geq \varepsilon_2 \geq \varepsilon_3$ , at the tension peak for the RVE with the cycling, we have

$$\varepsilon_1 \geq \varepsilon_{ii}, \quad \varepsilon_3 \leq \varepsilon_{ii} \quad i = 1, 2, 3 \quad (14)$$

where  $\varepsilon_1$ ,  $\varepsilon_2$  and  $\varepsilon_3$  are the first, second and third principal strains, respectively;  $\varepsilon_{ii}$  is the normal strains. Accordingly, comparing the mean normal strain along the macro loading direction  $l$ , mean first principal strain and the

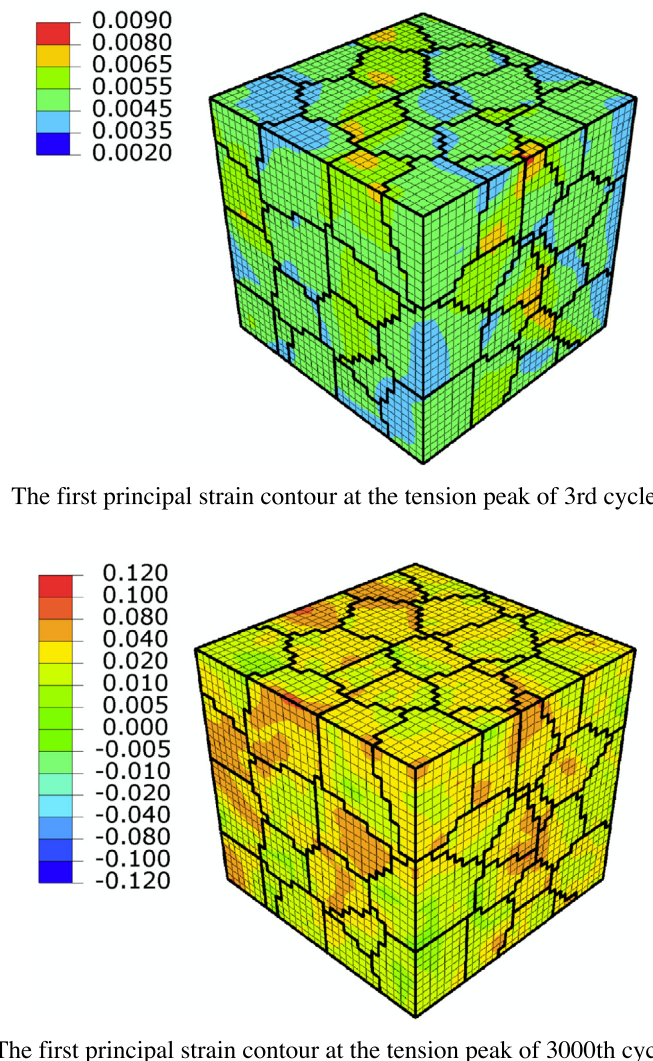


**Fig. 19.** The iso-contours of first principal strain for a strain amplitude of 0.005 at the tension peaks of the 3rd and the 3000th cycle.

maximum first principal strain for the RVE of polycrystalline aggregation, we obtain the following inequalities

$$\max_{RVE}(\varepsilon_1) \geq \sum_{k=1}^{n_{RVE}} (\varepsilon_1)_k p_k \geq \sum_{k=1}^{n_{RVE}} (\varepsilon_{1l})_k p_k \quad (15)$$

or simply

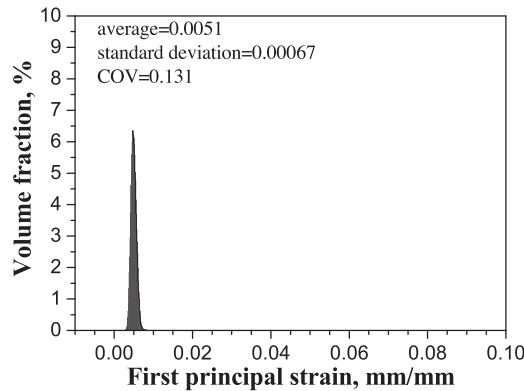
$$\varepsilon_{1\max} \geq \bar{\varepsilon}_1 \geq \bar{\varepsilon}_{1l} \quad (15')$$

$\bar{\varepsilon}_1 \geq \bar{\varepsilon}_{1l}$  is caused by the inhomogeneity of the material giving rise to the deflection of principal direction. Further, it can be presumed that the evolution of inhomogeneous deformation will affect the parameters  $\bar{\varepsilon}_1$  and  $\varepsilon_{1\max}$ , since the principal strain may increase with the deflection of principal direction.

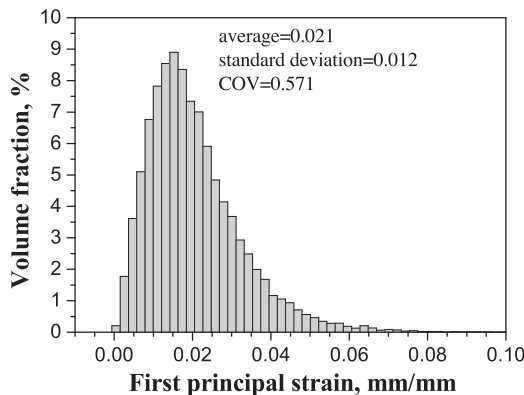
To verify this presumption, the deflection angle between the first principal strain and the longitudinal loading direction is calculated, which characterizes the rotation of the first principal strain. The results reflecting variance of the deflection of the first principal strain are given in Fig. 18, which displays the distributions of the first principal direction calculated at the tension peaks of the 3rd and the 3000th cycle at a strain amplitude of 0.005. One can see that the deflection of the first principal direction increases remarkably in the course of the cyclic

process. Correspondingly, Figs. 19 and 20 show the distribution of the first principal strain as iso-contours and histograms, respectively, at the tension peaks of the 3rd and the 3000th cycle for the same strain amplitude. From these figures, we similarly observe that both the statistical average and the standard deviation of the first principal strain increase considerably from the 3rd to the 3000th cycle. The result that the average of the first principal strain grows with cycle number fits with Eq. (15). For the reason of page limitations, only the results for a strain amplitude of 0.005 as displayed in Figs. 18–20 are discussed. The results are similar for other strain amplitudes from 0.45% to 1.3%.

Figs. 21 and 22 display the variations of the average,  $\bar{\varepsilon}_1$ , and the maximum,  $\varepsilon_{1\max}$ , of the first principal micro strain under different strain amplitudes  $\frac{1}{2}\Delta E_t$ , at the tension peak with cycling. The two figures signify that both parameters  $\bar{\varepsilon}_1$  and  $\varepsilon_{1\max}$  at the tension peak increase monotonically with the cycle number, similarly to  $\hat{\varepsilon}_{1l}$  (cf. Fig. 15). The curves in Fig. 22 are less in smooth, however, than those shown in Figs. 15 and 21 which might result from the changes of element location for  $\varepsilon_{1\max}$ . As for the local longitudinal strains, we set a series of limit values of the mean first principal strain  $\bar{\varepsilon}_1$ , denoted as  $\bar{\varepsilon}_{1l'}$ , and a series of limit values of the maximum first principal strain  $\varepsilon_{1\max}$ , denoted



The distribution of the first principal strain at the tension peak of the 3rd cycle



The distribution of the first principal strain at the tension peak of the 3000th cycle

Fig. 20. The histogram of the first principal strain at the tension peaks of the 3rd and the 3000th cycle for a strain amplitude 0.005.

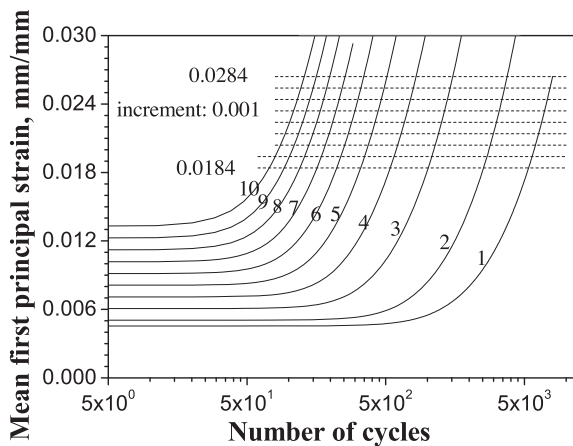


**Fig. 21.** The variations of average micro first principal strain  $\bar{\epsilon}_1$  calculated under different strain amplitudes at the tension peak for the RVE with the cycle number. The transverse lines mean various critical value of the first principal strain.

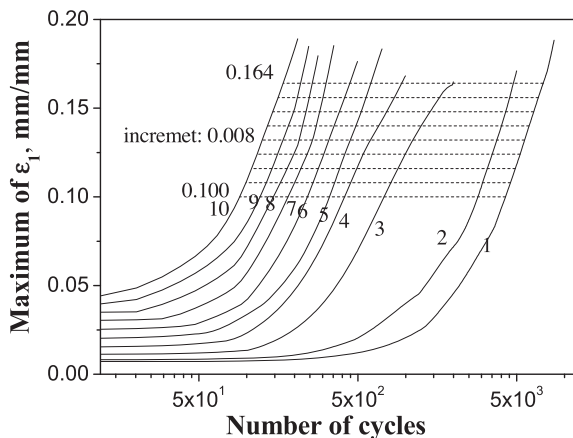


**Fig. 22.** The variations of the maximum of first principal micro strain,  $\epsilon_{1\max}$ , for different strain amplitudes  $\frac{1}{2}\Delta E_t$ , at the tension peak with cycling.

as  $\epsilon_{1\max}^f$  which is displayed by horizontal lines in Figs. 21 and 22. For both figures, the number of lines is 9, the specified data for  $\bar{\epsilon}_1^f$  range from 0.0184 to 0.0264 with

increment 0.001, and the specified data for  $\epsilon_{1\max}^f$  from 0.100 to 0.164 with increment 0.008 (the elongation for the strength of GH4169 under monotonic uniaxial tension is 0.13–0.2; Wu et al., 2008, page 381). In both figures, the intersections of these lines with the curves of the mean first principal strain vs. the cycle number and the maximum first principal strain vs. the cycle number, respectively, can be determined. Therefore, values of the fatigue cycle number for a specific strain amplitude can be predicted in dependence on the assumed limit values of mean  $\bar{\epsilon}_1^f$  and maximum  $\epsilon_{1\max}^f$ . These data are listed in Tables 5 and 6, respectively.

Furthermore, families of curves for fatigue life for various limit values based on analysis of the average and maximum first principal micro strain are plotted as in Figs. 23 and 24, based on Tables 5 and 6 as done above for longitudinal strain (cf. Fig. 16). Introducing the experimental fatigue life data (Wu et al., 2008, page 511) for the strain amplitudes: 0.45%, 0.6%, 0.8%, 0.9, 1.0% and 1.3% into Figs. 23 and 24, one can observe that the predicted fatigue life curves for the mean  $\bar{\epsilon}_1^f$  or maximum  $\epsilon_{1\max}^f$  are reasonable and close to the prediction as presented in Fig. 16 above by using Eq. (13). Taking the predicted data of fatigue lives for  $\bar{\epsilon}_1^f$  equal to 0.0284 (maximum), 0.0224 (median) and 0.0184 (minimum), respectively, in Fig. 23, and for  $\epsilon_{1\max}^f$  equal to 0.164 (maximum), 0.132 (median) and 0.100 (minimum), respectively, in Fig. 24, the comparisons with experimental fatigue lives can be rendered in Figs. 25 and 26. The model predictions based on the average,  $\bar{\epsilon}_1$ , and maximum,  $\epsilon_{1\max}$ , of the first principal strain are almost within the factor-of-two lines. Thus, it is clear that both predictions are very similar to those based on  $\hat{\epsilon}_{II}$ . The parameters  $\bar{\epsilon}_1$  and  $\epsilon_{1\max}$  representing the level of the principal stretch reached at the grain scale can also be regarded as proper indicators for fatigue crack initiation occurring in the material under uniaxial fatigue loading. Therefore, the parameters  $\hat{\epsilon}_{II}$ ,  $\bar{\epsilon}_1$  and  $\epsilon_{1\max}$  describe the same fact, and from the present analyses compared with experimental data they can be regarded as the parameters to judge fatigue failure for a material under uniaxial fatigue loading.

If the constitutive behavior and the microstructure of the material are known, fatigue life curves can be evaluated prior to the fatigue experiments in dependence of one critical parameter, which can be determined by an LCF test at only one strain amplitude. Therefore, the criterion for fatigue failure described by Eq. (13) can be recast as

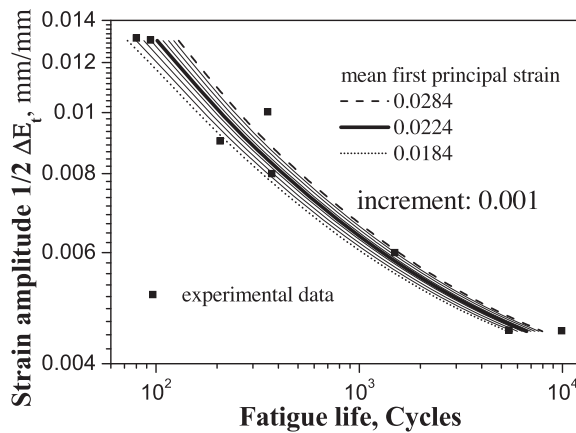
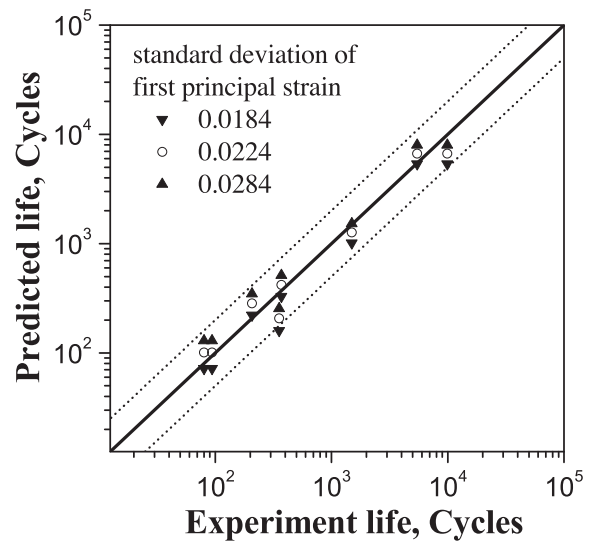
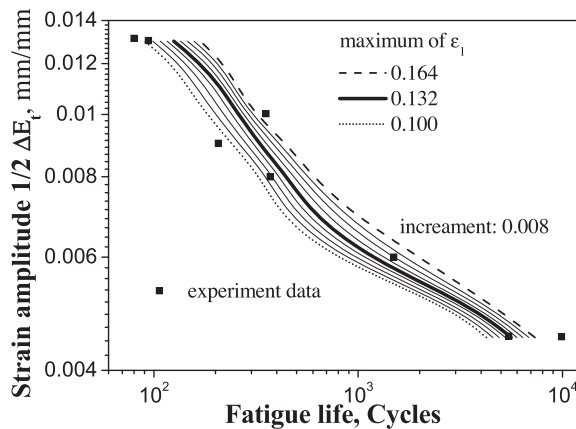
**Table 5**  
Fatigue life prediction for various critical values of the mean first principal strain.

$\bar{\epsilon}_1^f = \frac{1}{2}\Delta E_t$ (%)	.0184	.0194	.0204	.0214	.0224	.0254	.0264	.0274	.0284
$N_f$									
1.3	72	80	87	94	101	108	115	122	129
1.2	93	101	110	118	126	134	142	150	158
1.1	120	130	140	149	159	169	178	188	197
1.0	160	172	184	196	207	219	231	243	255
0.9	222	238	253	269	284	300	316	331	347
0.8	330	352	375	397	420	442	465	488	511
0.7	540	575	610	646	682	718	755	792	829
0.6	1013	1076	1139	1202	1265	1329	1394	1458	1523
0.5	2539	2689	2839	2990	3142	3294	3447	3601	3757
0.45	5363	5686	6010	6336	6663	6991	7321	7653	7987

**Table 6**

Fatigue life prediction for various critical values of the maximum first principal strain.

$\bar{\varepsilon}_{1\max f} = \frac{1}{2}\Delta E_t$ (%)	.100	.108	.116	.124	.132	.140	.148	.156	.164
$N_f$									
1.3	90	99	107	116	125	135	146	157	169
1.2	121	133	144	156	169	183	197	208	219
1.1	147	163	180	197	213	225	236	247	259
1.0	182	200	219	240	259	274	288	302	316
0.9	241	261	283	305	329	355	383	414	445
0.8	332	357	385	414	448	487	526	524	603
0.7	413	451	493	541	599	677	759	849	945
0.6	731	808	896	994	1110	1252	1426	1630	1985
0.5	2853	3052	3272	3503	3751	4009	4264	4516	4766
0.45	4250	4570	4908	5253	5606	5989	6402	6844	7335

**Fig. 23.** The fatigue life curves of cycle number versus strain amplitude for various limit values of the statistical mean first principal strain according to Table 5 comparing with experimental fatigue lives data (Wu et al., 2008, page 511).**Fig. 25.** The comparison of the predicted data calculated by various limit value of the statistical first principal strain, respectively, 0.0284 (maximum), 0.0224 (median) and 0.0184 (minimum), with experimental fatigue data.**Fig. 24.** The fatigue life curves of cycle number versus strain amplitude for various limit values of the maximum first principal strain according to Table 6 comparing with experimental fatigue lives data (Wu et al., 2008, page 511).

$$\bar{\varepsilon}_1 = \bar{\varepsilon}_{1\text{fatigue}} \quad \text{or} \quad \varepsilon_{1\max} = \varepsilon_{1\max\text{fatigue}} \quad (16)$$

where,  $\bar{\varepsilon}_{1\text{fatigue}}$  and  $\varepsilon_{1\max\text{fatigue}}$  are the critical values for parameters  $\bar{\varepsilon}_1$  and  $\varepsilon_{1\max}$  respectively. Since it has been verified in Figs. 15 and 16, Figs. 21–24, respectively, that longitudinal strains or maximum principal strains control failure by LCF, similar abilities of the accumulated effective plastic strain,  $p$ , or plastic work to predict failure can be examined. Note that the key property of longitudinal strains and maximum principal strains comprises that they reach critical values which are independent of the amplitude of applied strain and can be correlated to failure, see Figs. 15, 21 and 22. Whether  $p$  is suitable as fatigue parameter depends on a comparable behavior. From the above simulations, we can obtain the results of maximum accumulated effective plastic strain with the cycle number under various applied strain amplitudes, which is



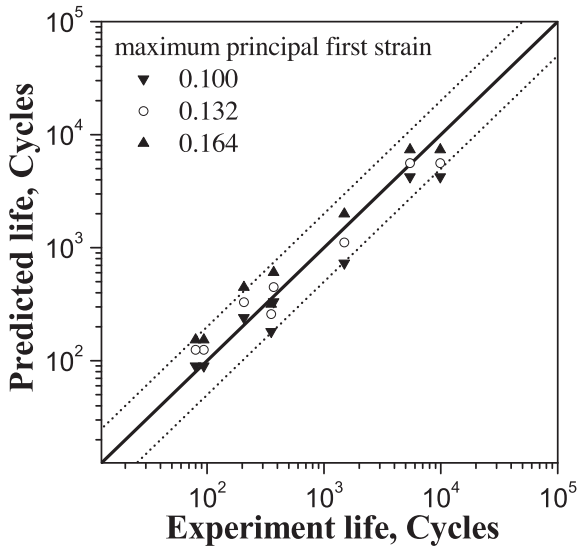


**Fig. 26.** The comparison of the predicted data calculated by various limit value of the maximum first principal strain, respectively, 0.164 (maximum), 0.132 (median) and 0.100 (minimum), with experimental fatigue data.

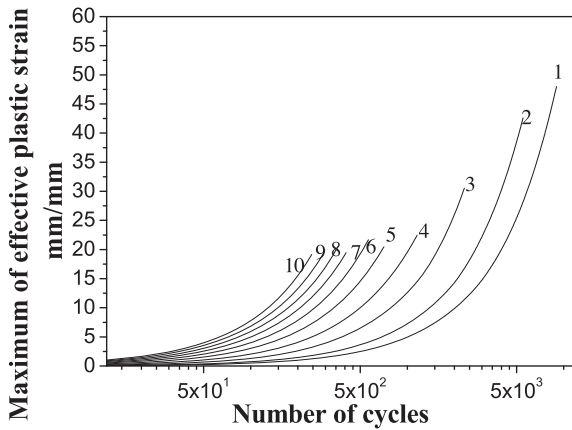


**Fig. 27.** The evolution and variation of the effective plastic strain,  $p$ , with number of cycles for different strain amplitudes at the tension peak. The curve numbers are identical to those in Fig. 15.

displayed in Fig. 27. The numbering of curves is the same as in Fig. 15. Comparing the two figures reveals that the attained values of  $p$  around the points of failure depend quite significantly on the amplitude of applied strain, which makes  $p$  unqualified for an LCF failure criterion. The same obviously holds for the plastic work.

### 3.5. Determination of the critical value for fatigue failure

The parameters of fatigue initiation  $\hat{\epsilon}_{fatigue}$ ,  $\bar{\epsilon}_{1fatigue}$  and  $\epsilon_{1maxfatigue}$  can be determined by the corresponding families of curves introduced above in combination with error analysis. The difference between experimental and predicted lives can be described assigned to some error value,

$$\text{Error}_1 = \sqrt{\sum_i \left( \frac{N_{f\_exp} - N_{f\_sim}}{N_{f\_exp}} \right)^2_i},$$

$$\text{Error}_2 = \max_i \left( \left| \frac{N_{f\_exp} - N_{f\_sim}}{N_{f\_exp}} \right|_i \right), \quad (17)$$

where,  $N_{f\_exp}$  and  $N_{f\_sim}$  denote the fatigue lives by experiment and numerical simulations, respectively;  $i$  is the index with respect to the corresponding strain amplitude. Using these definitions, the errors for the predictions of fatigue life by applying the fatigue initiation parameters  $\hat{\epsilon}_{fatigue}$ ,  $\bar{\epsilon}_{1fatigue}$  and  $\epsilon_{1maxfatigue}$  are listed in Table 7, Table 8 and Table 9, respectively. From this tables one can chose the best parameters by which the error is the lowest. Difference between the definitions of Error<sub>1</sub> and Error<sub>2</sub> may result in a different parameter choice (see Tables 7–9, where the bold figures are the minimum values evaluated by respective error functions). For example, if  $\bar{\epsilon}_{1fatigue}$  is applied, its critical value is 0.0204 or 0.224 depending on that the error evaluation using Error<sub>1</sub> or Error<sub>2</sub> is adopted.

According to the error analysis of this section, one can realize that the three fatigue criteria reflect the same or very similar fatigue law, namely that the fatigue crack initiation may be regarded as mainly dependent on the local strain, representing by  $\hat{\epsilon}_{II}$ ,  $\bar{\epsilon}_{1f}$  or  $\epsilon_{1max}$  reaching a critical value. Currently we cannot conclude which criterion is the best; it needs to be investigated further.

According to the results exhibited in this section and last section, it is found the family of curves obtained by the present methodology shown in Figs. 16, 23 and 24

**Table 7**  
Error for fatigue life prediction evaluated by using various  $\hat{\epsilon}_{II}$ .

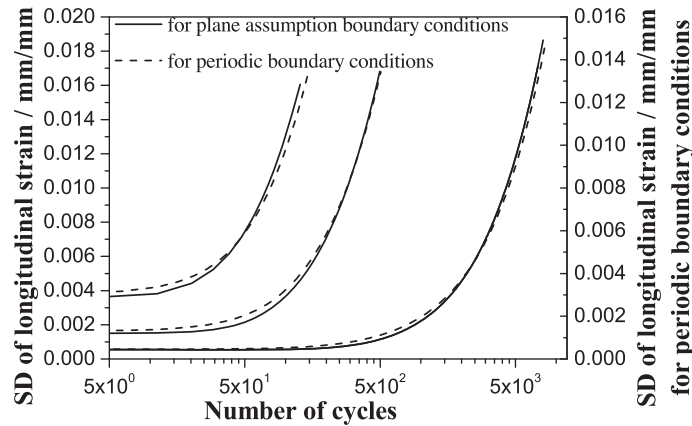
$\hat{\epsilon}_{II}$	.0126	.0132	.0138	.0144	.0150	.0156	.0162	.0168	.0174	.0180	.0186
Error <sub>1</sub> (%)	<b>63</b>	65	68	73	79	87	96	105	115	125	136
Error <sub>2</sub> (%)	47	45	42	<b>41</b>	48	55	62	69	76	84	91

**Table 8**  
Error for fatigue life prediction evaluated by using various  $\bar{\epsilon}_{1f}$ .

$\bar{\epsilon}_{1f}$	.0184	.0194	.0204	.0214	.0224	.0234	.0244	.0254	.0264
Error <sub>1</sub> (%)	66	61	<b>59</b>	60	65	72	81	92	103
Error <sub>2</sub> (%)	55	51	48	45	<b>41</b>	45	52	60	68

**Table 9**Error for fatigue life prediction evaluated by using various  $\varepsilon_{1\max f}$ .

$\varepsilon_{1\max f}$	.100	.108	.116	.124	.132	.140	.148	.156	.164
Error <sub>1</sub> (%)	76	70	<b>67</b>	68	73	83	98	117	140
Error <sub>2</sub> (%)	51	46	<b>40</b>	48	59	71	85	100	115

**Fig. 28.** The comparison of variation of the standard deviation (SD)  $\hat{\varepsilon}_{II}$  of the RVE under the strain amplitudes 0.045%, 0.8% and 1.3% at the tension peak with cycle number, from which one can see that the curves for two boundary conditions are similar.

can describe the law of fatigue life of the material well, and the errors (Error<sub>2</sub>) for lives prediction shown in Tables 7–9 demonstrate that no matter what strain amplitude is referred the proper predicting curve always can be obtained. This implies that the appropriate critical values for above three criteria can be determined by the cyclic experiments with only one strain amplitude.

#### 4. Discussions

In the present paper, only the low-cycle fatigue life of a polycrystalline metal under the condition of uniaxial tensile-compressive cycle loading is investigated without consideration of the complicated loading path, multiaxial stress state. Compared with the fatigue life of materials loaded by uniaxial tensile-compressive cycles, the fatigue life of a metallic material tested by multiaxial and non-proportional loading is substantially different. Although the strain level at the loading peak is the same, the difference in fatigue life may reach about ten times for specimens tested under different loading paths. In the future, the LCF life of materials subjected to proportional or non-proportional multiaxial loading needs more attention. A failure criterion based on the proposed methodology, taking into account further effects of the macroscopic stress state and the loading paths, is deemed promising. For example, the maximum shear strain should be considered to measure the deformation at the grain level, and the influence of stress state on material failure mode also should be considered. Respective investigations involving cyclic shearing and multiaxial loading have been performed and they will be reported in a forthcoming paper.

The boundary conditions which have been used in the present paper consume about 50% less computational time

compared with periodic boundary conditions (Michel et al., 1999). The resulting differences are small, however, as Fig. 28 shows with respect to the variation of the standard deviation,  $\hat{\varepsilon}_{II}$ , for strain amplitudes of 0.045%, 0.8% and 1.3%. More details about the difference between two kind of boundary conditions are omitted here because of page limitations.

Time consumption by the cyclic simulations is an issue for the present methodology. Hence, some cycle jumping technique should be considered in future investigations.

#### 5. Conclusions

According to the investigation of this paper, the following conclusions can be obtained:

- (1) In a polycrystalline metal under global uniaxial tensile-compressive cyclic loading, the deflection of the local first principal direction to the longitudinal loading direction changes and its average increases with cycle number. As a result, the statistical standard deviation of local longitudinal strain  $\hat{\varepsilon}_{II}$  and the maximum  $\varepsilon_{1\max}$  and statistical average of local first principal strain  $\bar{\varepsilon}_1$  increase monotonically and similarly with increasing cycle number.
- (2) According to the analysis of microscopic strain distributions in the RVE, it is confirmed that  $\hat{\varepsilon}_{II}$ ,  $\varepsilon_{1\max}$  and  $\bar{\varepsilon}_1$  at the tension peak of cyclic loading can be considered as reaching respective limit values when fatigue failure initiation of the material occurs, which are independent of the amplitude of applied strain and can be regarded as material constants to predict failure by low-cycle fatigue.

- (3) Using the presented methodology, the curves of fatigue lives for a metallic material under specified cycle strain amplitudes can be predicted in dependence on one parameter values prior to the fatigue experiment, provided that the constitutive behavior and the microstructure of the material are known. The appropriate critical values can be determined by the cyclic experiments with only one strain amplitude.

## Acknowledgments

This research was supported by the National Natural Scientific Foundation of China (Fund Nos. 90815001, 11072064, 11272094 and 11472085) and the Key Project of Guangxi Science and Technology Lab Center (Fund No. LGZX201101). These financial supports are gratefully acknowledged. The discussions with Drs. Duokui Yu and Xiangping Wang on the fatigue of GH4169 in aero engine are highly appreciated.

## References

- Abdeljaoued, D., Naceur, B.I., Saï, K., Cailletaud, G., 2009. A new polycrystalline plasticity model to improve ratcheting strain prediction. *Mech. Res. Commun.* 36, 309–315.
- Armstrong, P.J., Frederick, C. O., 1966. A mathematical representation of the multiaxial Bauschinger effect. Report RD/B/N731, CEBG, Central Electricity Generating Board, Berkeley, UK.
- Asaro, R.J., Rice, J.R., 1977. Strain localization in ductile single crystals. *J. Mech. Phys. Solids* 25, 309–338.
- Barbe, F., Decker, L., Jeulin, D., Cailletaud, G., 2001. Intergranular and intragranular behavior of polycrystalline aggregates. Part 1: FE model. *Int. J. Plast* 17, 513–536.
- Brocks, W., Steglich, D., 2007. Hybrid Methods, in: *Comprehensive Structural Integrity* (Eds. Milne, I., Ritchie, R.O., Karihaloo, B.), Fracture of Materials from Nano to Macro, vol. 11, 107–136.
- Buciumeanu, M., Palaghian, L., Miranda, A.S., Silva, F.S., 2011. Fatigue life predictions including the Bauschinger effect. *Int. J. Fatigue* 33, 145–152.
- Cailletaud, G., 1992. A micromechanical approach to inelastic behavior of metals. *Int. J. Plast* 8, 55–73.
- Chaboche, J.L., 2008. A review of some plasticity and viscoplasticity constitutive theories. *Int. J. Plast* 24, 1642–1693.
- Chaboche, J.L., Kanouté, P., Azzouz, F., 2012. Cyclic inelastic constitutive equations and their impact on the fatigue life predictions. *Int. J. Plast* 35, 44–66.
- Chang, Y.W., Asaro, R.J., 1981. An experimental study of shear localization in aluminum-copper single crystals. *Acta Metall.* 29, 241–257.
- Coffin Jr., L.F., 1954 (A study of the effect of cyclic thermal stresses on a ductile metal). *Trans. ASME* 76, 931–950.
- Dingreville, R., Battaile, C.C., Brewer, L.N., Holm, E.A., Boyce, B.L., 2010. The effect of microstructural representation on simulations of microplastic ratcheting. *Int. J. Plast* 26, 617–633.
- Dunne, F.P.E., 2014. Fatigue crack nucleation: mechanistic modelling across the length scales. *Curr. Opin. Solid State Mater. Sci.* 18, 170–179.
- Dunne, F.P.E., Wilkinson, A.J., Allen, R., 2007. Experimental and computational studies of low cycle fatigue crack nucleation in a polycrystal. *Int. J. Plast* 23, 273–295.
- Feng, L., Zhang, G., Zhang, K.S., 2004. Discussion of cyclic plasticity and viscoplasticity of single crystal nickel-based superalloy in large strain analysis: comparison of anisotropic macroscopic model and crystallographic model. *Int. J. Mech. Sci.* 46, 1157–1171.
- Guerchais, R., Robert, C., Morel, F., Saintier, N., 2014. Micromechanical study of the loading path effect in high cycle fatigue. *Int. J. Fatigue* 59, 64–75.
- Guilhem, Y., Basseville, S., Curtit, F., Stéphan, J.M., Cailletaud, G., 2010. Investigation of the effect of grain clusters on fatigue crack initiation in polycrystals. *Int. J. Fatigue* 32, 1748–1763.
- Hill, R., Rice, J.R., 1972. Constitutive analysis of elastic-plastic crystal at arbitrary strain. *J. Mech. Phys. Solids* 20, 401–413.
- Huang, M.S., Tong, J., Li, Z.H., 2014. A study of fatigue crack tip characteristics using discrete dislocation dynamics. *Int. J. Plast* 54, 229–246.
- Hu, G.J., Huang, S.H., Lu, D.M., Zhong, X.C., Li, Z.H., Brocks, W., Zhang, K.S., 2015. Subsequent yielding of polycrystalline aluminum after cyclic tension-compression analyzed by experiments and simulations. *Int. J. Solids Struct.* 56–57, 142–153.
- Hutchinson, J.W., 1970. Elastic-plastic behaviour of polycrystalline metals and composites. *Proc. R. Soc. Lond. A* 319, 247–272.
- Hutchinson, J.W., 1976. Bounds and self-consistent estimates for creep of polycrystalline materials. *Proc. R. Soc. Lond. A* 348, 101–127.
- Ince, A., Glinka, G., 2014. A generalized fatigue damage parameter for multiaxial fatigue life prediction under proportional and non-proportional loadings. *Int. J. Fatigue* 62, 34–41.
- Jiang, Y.Y., Ott, W., Baum, C., Vormwald, M., Nowack, H., 2009. Fatigue life predictions by integrating EVICD fatigue damage model and an advanced cyclic plasticity theory. *Int. J. Plast* 25, 780–801.
- Ju, J.W., Chen, T.M., 1994. Micromechanics and effective elastoplastic behavior of two-phase metal matrix composites. *J. Eng. Mater. Technol. ASME* 116, 310–318.
- Ju, J.W., Tseng, K.H., 1996. Effective elastoplastic behavior of two-phase ductile matrix composites: a micromechanical framework. *Int. J. Solids Struct.* 33 (29), 4267–4291.
- Ju, J.W., Sun, L.Z., 2001. Effective elastoplastic behavior of metal matrix composites containing randomly located aligned spheroidal inhomogeneities. Part I: micromechanics-based formulation. *Int. J. Solids Struct.* 38 (2), 183–201.
- Kalidindi, S.R., Bronkhorst, C.A., Anand, L., 1992. Crystallographic texture evolution in bulk deformation processing of FCC metals. *J. Mech. Phys. Solids* 40, 537–569.
- Kanit, T., Forest, S., Galliet, I., Mounoury, V., Jeulin, D., 2003. Determination of the size of the representative volume element for random composites: statistical and numerical approach. *Int. J. Solids Struct.* 40, 3647–3679.
- Keshavarz, S., Ghosh, S., 2013. Multi-scale crystal plasticity finite element model approach to modeling nickel-based superalloys. *Acta Mater.* 61, 6549–6561.
- Li, H.Y., Kong, Y.H., Chen, G.S., Xie, L.X., Zhu, S.G., Sheng, X., 2013. Effect of different processing technologies and heat treatments on the microstructure and creep behavior of GH4169 superalloy. *Mater. Sci. Eng., A* 582, 368–373.
- Maniatty, A.M., Dawson, P.R., Lee, Y.S., 1992. A time integration algorithm for elasto-viscoplastic cubic crystals applied to modeling polycrystalline deformation. *Int. J. Numer. Methods Eng.* 35, 1565–1588.
- Manonukul, A., Dunne, F.P.E., 2004. High- and low-cycle fatigue crack initiation using polycrystal plasticity. *Proc. R. Soc. A* 460, 1881–1903.
- Manson, S.S., 1953. Behavior of materials under conditions of thermal stress. In: *Heat Transfer Symposium*, University of Michigan Engineering Research Institute, MI, 9–75.
- Masing, G., 1926. Eigenspannungen und Verfestigung beim Messing. In: *Proceedings of the 2nd International Congress on Applied Mechanics*, Zürich, 332–335.
- McDowell, D.L., Dunne, F.P.E., 2010. Microstructure-sensitive computational modeling of fatigue crack formation. *Int. J. Fatigue* 32, 1521–1542.
- Michel, J.C., Moulinec, H., Suquet, P., 1999. Effective properties of composite materials with periodic microstructure: a computational approach. *Comput. Methods Appl. Mech. Eng.* 172, 109–143.
- Naderi, M., Hoseini, S.H., Khonsari, M.M., 2013. Probabilistic simulation of fatigue damage and life scatter of metallic components. *Int. J. Plast* 43, 101–115.
- Needleman, A., Asaro, R.J., Lemonds, J., Peirce, D., 1985. Finite element analysis of crystalline solids. *Comput. Methods Appl. Mech. Eng.* 52, 689–708.
- Ni, K., Mahadevan, S., 2004. Strain-based probabilistic fatigue life prediction of spot-welded joints. *Int. J. Fatigue* 26, 63–772.
- Pan, J., Rice, J.R., 1983. Rate sensitivity of plastic flow and implications for yield-surface vertices. *Int. J. Solids Struct.* 19, 973–987.
- Peirce, D., Asaro, R.J., Needleman, A., 1983. Material rate dependence and localized deformation in crystalline solids. *Acta Metall.* 31, 1951–1976.
- Przybyla, C.P., McDowell, D.L., 2010. Microstructure-sensitive extreme value probabilities for high cycle fatigue of Ni-base superalloy IN100. *Int. J. Plast* 26 (3), 372–394.

- Roy, S.C., Goyal, S., Sandhya, R., Ray, S.K., 2012. Low cycle fatigue life prediction of 316L (N) stainless steel based on cyclic elasto-plastic response. *Nucl. Eng. Des.* 253, 219–225.
- Sangid, M.D., Maier, H.J., Sehitoglu, H., 2011. An energy-based microstructure model to account for fatigue scatter in polycrystals. *J. Mech. Phys. Solids* 59, 595–609.
- Sarma, G., Zacharia, G., 1999. Integration algorithm for modeling the elastoviscoplastic response of polycrystalline materials. *J. Mech. Phys. Solids* 47, 1219–1238.
- Shenoy, M., Tjiptowidjojo, Y., McDowell, D., 2008. Microstructure-sensitive modeling of polycrystalline IN 100. *Int. J. Plast.* 24, 1694–1730.
- Sun, L.Z., Ju, J.W., Liu, H.T., 2003a. Elastoplastic modeling of metal matrix composites with evolutionary particle debonding. *Mech. Mater.* 35, 559–569.
- Sun, L.Z., Liu, H.T., Ju, J.W., 2003b. Effect of particle cracking on elastoplastic behavior of metal matrix composites. *Int. J. Numer. Methods Eng.* 56, 2183–2198.
- Sweeney, C.A., O'Brien, B., Dunne, F.P.E., McHugh, P.E., Leen, S.B., 2014a. Strain-gradient modelling of grain size effects on fatigue of CoCr alloy. *Acta Mater.* 78, 341–353.
- Sweeney, C.A., O'Brien, B., McHugh, P.E., Leen, S.B., 2014b. Experimental characterisation for micromechanical modelling of CoCr stent fatigue. *Biomaterials* 35, 36–48.
- Sweeney, C.A., Vorster, W., Leen, S.B., Sakurada, E., McHugh, P.E., Dunne, F.P.E., 2013. The role of elastic anisotropy, length scale and crystallographic slip in fatigue crack nucleation. *J. Mech. Phys. Solids* 61, 1224–1240.
- Taheri, S., Hauet, A., Taleb, L., Kpodekon, C., 2011. Micro-macro investigations about the fatigue behavior of pre-hardened 304L steel. *Int. J. Plast.* 27, 1981–2004.
- Wu, X.R., Yang, S.J., Han, X.P., Liu, S.L., Liu, Q.S., Lu, K.R., et al., 2008. *Data Manual for Materials of Aero-Engine, Aircraft Engine Design Data Manual for Materials*. Aviation Industry Press, China (In Chinese).
- Wu, Z.R., Hu, X.T., Song, Y.D., 2014. Multiaxial fatigue life prediction for titanium alloy TC4 under proportional and nonproportional loading. *Int. J. Fatigue* 59, 170–175.
- Ye, D.Y., Wang, Z.L., 2001. A new approach to low-cycle fatigue damage based on exhaustion of static toughness and dissipation of cyclic plastic strain energy during fatigue. *Int. J. Fatigue* 23 (8), 679–687.
- Zhang, K.S., 2004. Microscopic heterogeneity and macroscopic mechanical behavior of a polycrystalline material. *Acta. Mech. Sin.* 36, 714–723, In Chinese.
- Zhang, K.S., Wu, M.S., Feng, R., 2005. Simulation of microplasticity-induced deformation in uniaxially strained ceramics by 3-D Voronoi polycrystal modeling. *Int. J. Plast.* 21, 801–834.
- Zhang, K.S., Shi, Y.K., Xu, L.B., Yu, D.K., 2011. Anisotropy of yielding/hardening and micro inhomogeneity of deforming/rotating for a polycrystalline metal under cyclic tension–compression. *Acta Metall. Sin.* 47, 1232–1300, In Chinese.
- Zhang, K.S., Shi, Y.K., Ju, J.W., 2013. Grain-level statistical plasticity analysis on strain cycle fatigue of a FCC metal. *Mech. Mater.* 64, 76–90.
- Zhu, H.X., Zhang, P., Balint, D., Thorpe, S.M., Elliott, J.A., Windle, A.H., Lin, J., 2014. The effects of regularity on the geometrical properties of Voronoi tessellations. *Phys. A* 406, 42–58.